The Journal of Undergraduate Research in Physics

VOLUME 10, NUMBER 2

APRIL, 1992

Published by the Physics Department of Guilford College
for
The American Institute of Physics and The Society of Physics Students

THE JOURNAL OF UNDERGRADUATE RESEARCH IN PHYSICS

This journal is devoted to research work done by undergraduate students in physics and its related fields. It is to be a vehicle for the exchange of ideas and information by undergraduate students. Information for students wishing to submit manuscripts for possible inclusion in the Journal follows.

ELIGIBILITY

The author(s) must have performed all work reported in the paper as an undergraduate student(s). The subject matter of the paper is open to any area of pure or applied physics or physics related field.

SPONSORSHIP

Each paper must be sponsored by a full-time faculty member of the department in which the research was done. A letter from the sponsor, certifying that the work was done by the author as an undergraduate and that the sponsor is willing to be acknowledged at the end of the paper, must accompany the manuscript if it is to be considered for publication.

SUBMISSION

Two copies of the manuscript, the letter from the sponsor and a telephone number where the author can be reached should be sent to:

Dr. Rexford E. Adelberger, Editor
THE JOURNAL OF UNDERGRADUATE
RESEARCH IN PHYSICS
Physics Department
Guilford College
Greensboro, NC 27410

FORM

The manuscript should be typed, double spaced, on 8 1/2 x 11 inch sheets. Margins of about 1.5 inches should be left on the top, sides, and bottom of each page. Papers should be limited to fifteen pages of text in addition to an abstract (not to exceed 250 words) and appropriate drawings, pictures, and tables. Manuscripts may be submitted on a disk that can be read by a MacIntosh™. The files must be compatible with MacWrite™ or MicroSoft Word™. Illustrations should be in a MacDraw™ or MacPaint™ PICT format.

ILLUSTRATIONS

Line drawings should be made with black ink on plain white paper. Each figure or table must be on a separate sheet. Photographs must have a high gloss finish.

CAPTIONS

A brief caption should be provided for each illustration or table, but it should not be part of the figure. The captions should be listed together at the end of the manuscript

EQUATIONS

Equations should appear on separate lines, and may be written in black ink.

FOOTNOTES

Footnotes should be typed, double spaced and grouped together in sequence at the end of the manuscript.

PREPARING A MANUSCRIPT

A more detailed set of instructions for authors wishing to prepare manuscripts for publication in the Journal of Undergraduate Research in Physics can be found in Volume 8 #1 which appeared in October of 1989.

SUBSCRIPTION INFORMATION

The Journal is published bianually, with issue # 1 appearing in October and issue # 2 in April of the next year. There are two issues per volume.

TYPE OF SUBSCRIBER	PRICE PER VOLUME
Individual	$US 5.00
Institution	$US 10.00

Foreign subscribers add $US 2.00 for surface postage, $US 10.00 for air freight.

Back issues may be purchased by sending $US 15.00 per volume to the editorial office.

To receive a subscription, send your name, address, and check made out to **The Journal of Undergraduate Research in Physics (JURP)** to the editorial office:

JURP
Physics Department
Guilford College
Greensboro, NC 27410

The Journal of Undergraduate Research in Physics is the sent to each member of the Society of Physics Students as part of their annual dues.

THE SPEED OF CARBON DIOXIDE BUBBLES RISING IN A GLASS OF BEER

Brett Davis and Brian Lightbourne
Physics Department
Valdosta State College
Valdosta, GA 31698
received April 20, 1991

ABSTRACT

The velocity of carbon dioxide bubbles rising in beer was measured using a stop-frame VCR. Our analysis of the motion gave a radius of $(3.1 \pm .1) \times 10^{-4}$ m. This result is approximately ten times larger than the calculated radius reported in a perviously published analysis of the bubble motion. [1]

1) W.A. DeZarn and M.A. Ward, The Journal of Undergraduate Research in Physics, 7, 1989, p. 49

INTRODUCTION

The motion of carbon dioxide bubbles rising in beer was analyzed by DeZarn and Ward [1] who stated that the radius of their bubble was on the order of 3.3×10^{-5} m. This seemed to be a very small value, so we decided to duplicate the experiment in order to investigate the bubble size.

In carbonated drinks, carbon dioxide is dissolved in the liquid. When the sealed container is opened, the pressure decreases to a level where CO_2 is released as bubbles. The bubbles begin to travel upward due to their buoyancy and accelerate until terminal velocity is reached. Terminal velocity was achieved almost instantaneously for the bubble diameters we observed. This behavior was also noted by C.F. Bohren. [2]

EXPERIMENTAL DESIGN

The beer was poured into a graduated cylinder which was illuminated by placing it on a slide viewing table. The position of the bubble was recording using a stop-frame video recorder with a frame speed of 1/30 of a second. The volume markings on the cylinder, converted to mks units, were used as a distance scale.

We obtained a rough estimate for the radius of the bubbles by viewing photographs of a ruler in the beer and utilizing the stop-frame VCR. Our visually estimated value for the radius was $(5 \pm 2) \times 10^{-4}$ m.

The position of the bubble was graphed as a function of time to determine the velocity. We found that some bubbles had a constant radius and velocity while others underwent an increase in size resulting in an acceleration. The change in pressure that the bubbles experience as they travel from the bottom to the top of the graduated cylinder is less than 0.1% of atmospheric pressure. Since this difference is negligible and the temperature of the liquid is uniform, it is reasonable to assume that a bubble can rise with a constant pressure, temperature, volume and number of moles, resulting in a zero acceleration. When we first poured the beer, we saw bubbles whose radius apparently increased. We assumed that this had to do with the concentration of carbon dioxide in the beer, which decreases with time after the beer is opened. We believe that the explanation given by C. F. Bohren [2] is correct: the acceleration is caused by diffusion of CO_2 into the bubble which increases the radius and therefore the buoyant force. This paper, however, is restricted to the case of a bubble with a constant radius and velocity.

RESULTS

Figure 1 is a plot of position versus time for a typical bubble. It had zero acceleration since a straight line gave an excellent fit to the data. The average velocity of the bubbles used for the analysis was $(7.3 \pm .1) \times 10^{-2}$ m/s.

DETERMINATION OF RADIUS

The equation of motion for is given by Newton's second law. The net force has two parts to it, the buoyant force and a drag force.

Brett Davis is a graduate of Valdosta State College. He is currently pursuing a Masters' degree in electrical engineering at the Southern College of Engineering. Brian Lightbourne graduated from Valdosta State College this year. He plans to return to Jamacia to start an agricultural business.

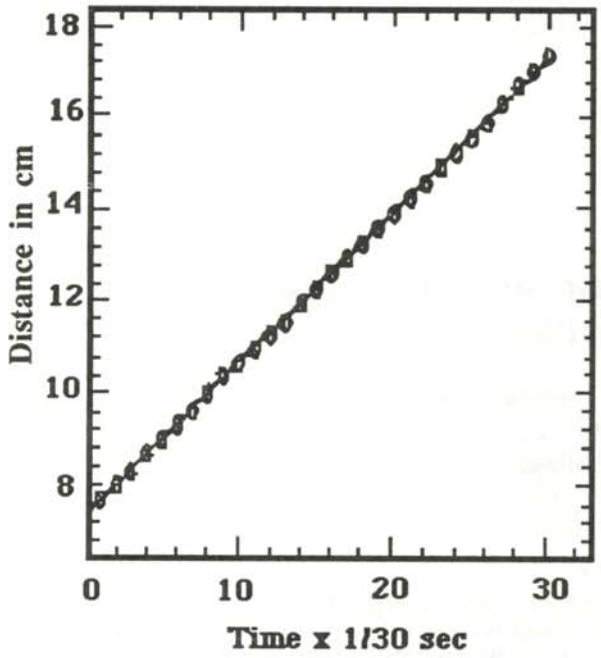

Figure 1
Typical distance time graph for one of the selected bubbles. The straight line shows that it is moving at a constant speed.

The buoyant force on the bubble is:

$$F_b = V (\rho_f - \rho_o) g \qquad (1)$$

where V is the volume, ρ_f is the density of the surrounding beer, ρ_o is the density of the carbon dioxide and g is the acceleration due to gravity. The density of the CO_2 in the bubble is approximately 500 times less than that of beer, therefore the ρ_o term is negligible and can be dropped.

As an object travels through a fluid, a drag force is exerted on it. This force is different depending on whether the fluid flow is laminar or turbulent. In order to determine which case applies, it is necessary to calculate the Reynolds number, R, for the flow:

$$R = 2 \rho_f v r / \eta \qquad (2)$$

Variabale	Description	Value
ρ_o	Density of CO_2	1.98 kg/m^3
ρ_f	Density of beer	1.007×10^3 kg/m^3
g	Accel. of gravity	9.8 m/sec^2
η	Viscosity of beer	1×10^{-3} Pa sec
η	Viscosity of alcohol	1.2×10^{-3} Pa sec

Table 1
Values of variables used in this experiment.

where v is the velocity, r is the radius of the bubble and η is the viscosity of the beer. We took the viscosity of beer to be that of water since beer is approximately 95% water and alcohol has approximately the same viscosity as water [3,5].

Table 1 shows the values for each variable used in the calculations. The Reynolds number we calculated using our initial estimate for the radius was 73. A sphere traveling through a fluid with a Reynolds number higher than approximately 10 requires the use of the equation[4]:

$$F_r = \rho_f \pi r^2 C_D v^2 / 2 \qquad (3)$$

The drag coefficient C_D was determined from a graph of drag coefficient vs Reynolds number for a sphere traveling through a fluid [4]. The graph was approximately linear for the region where the Reynolds number was less than 100. A least-square fit to the linear region of the graph yielded:

$$C_D = -1.14 \text{ Log}(R) + 3.43 \qquad (4)$$

From this equation we were able to calculate a value for the drag coefficient of the bubble. Since the bubble reaches terminal velocity almost instantaneously, the drag force (Equation 3) and the buoyant force (Equation 1 with the ρ_o dropped) can be set equal to each other and a solution obtained for the radius:

$$r = 3 C_D v^2 / (8 g) \qquad (5)$$

The radius was calculated from Equation 5 and substituted into Equation 2 to find a revised Reynolds number and the resulting drag coefficient was obtained from Equation 4. With this drag coefficient, a new radius was found from Equation 5. This iteration process was continued until the radius converged. Table 2 shows the values obtained for each iteration. A value of $(3.1 \pm .1) \times 10^{-4}$m was obtained for the radius

Our calculated value for the radius is much closer to the visually estimated radius of 5.0×10^{-4}m than DeZarn and Ward's [1] value of 3.3×10^{-5}m. We believe their value is too small. A bubble of that radius would be extremely difficult to observe. We did not find any evidence for the occurrence of any unusual thermodynamic processes. If we can obtain video equipment with sufficient resolution to allow the direct measurement of the radius, we plan to do further experiments focusing on the dynamics of bubbles that increase in size.

ACKNOWLEDGEMENTS

The authors would like to thank Dr. Frank Flaherty for his guidance and encouragement. We would also like to thank the faculty of the Physic, Astronomy and Engineering for their critique of our work.

REFERENCES

1. W.A. DeZarn and M.A. Ward, The Journal of Undergraduate Research in Physics, 7, 1, 1989 pp. 49-52.

2. Craig F. Bohren, Clouds in a Glass of Beer, Wiley, New York, 1987, p. 6.

Radius x 10^{-4}m	Reynolds #	Drag Coef	Radius x 10^{-4}m
5.00	73.2	1.3	2.65
2.65	38.7	1.62	3.28
3.28	48.1	1.51	3.07
3.07	44.9	1.55	3.14
3.14	45.9	1.54	3.11
3.11	45.6	1.53	3.12

Table 2

Results from the iterative process for finding the radius of the rising bubble.

3. Douglas C. Giancoli, Physics 2nd Edition, Prentice Hall Inc, New Jersey, 1985, p. 212 and p. 315.

4. David Halliday and Robert Resnick, Fundamentals of Physics Extended 3rd Edition, Wiley, New York, 1988, p. E6-2,3.

5. Mark's Standard Handbook for Mechanical Engineers 8th Edition, McGraw Hill 1978, pp. 3 - 36.

FACULTY SPONSOR

Dr. Frank A. Flaherty
Department of Physics, Astronomy and Geology
Valdosta State College
Valdosta, GA 31698

COMMENTS BY AUTHOR OF ORIGINAL PAPER

The major difference between the analysis of this experiment and what we did seems to be the value used for the viscosity of the beer. We got our value from the brewer at Stroh's Brewery. They told us that the value varied quite a bit among different beers. We used the value for the particular brand and style of beer we used in the experiment. Our value of 1.5x10^{-3} Pa sec. is a factor of almost 70 different from the value assumed in this experiment. The bubbles in our brand of beer seemed to be traveling at almost twice the speed as the ones observed in this experiment.

Perhaps the argument about the viscosity needs reviewing. At an extreme, the human body is 92% water, but definitely has a different viscosity than that of water. In a more serious tone, if one just examines closely the way that beer and water pour into a glass, one can see a difference in their flow.

William DeZarn 5/30/91

ATOMIC CONCENTRATION ANALYSIS FROM RUTHERFORD BACK-SCATTERING SPECTRA OF SAMPLES IMPLANTED TO HIGH DOSE

Ken Jensen *
Physics Department
Wright State University
Dayton, OH 45435
received May 7, 1992

ABSTRACT

A procedure for extracting stoichiometry relationships and atomic concentrations as a function of depth from Rutherford back scattering spectra of samples implanted to high dose is described. These relationships are applied to implanted SiO_2 samples by making assumptions about the post-implantation concentration in the sample.

INTRODUCTION

Rutherford back-scattering occurs when the collision between two objects is mediated by an inverse square force law such as that between two point charges. The final energy of the objects involved in the scattering can be deduced from the scattering angle and the usual energy and momentum conservation relationships for a two-body collision. [1] In Rutherford Back-scattering Spectrometry (RBS), a beam of ionized atoms, having fixed mass and incident energy, are directed onto a target, where they undergo collisions with the nuclei of the atoms in the target. The energy of each back-scattered particle is detected at a fixed angle. The number of back-scattered particles having a given energy is plotted vs that energy to produce the RBS spectrum. The energy detected for each back-scattered ion also reflects the 'frictional' energy lost to electrons while it goes into and comes out of the target material.

Figure 1 show two typical RBS spectra. The horizontal axis (channel number) is the energy of the incident particle. The yield is related to the number of target atoms per cm^2 and the energy is related to the depth of the atoms in the sample[1]. If the sample has a constant density, these relationships can be combined to give a volume concentration as of function of depth.

The leading edge is characterized by a near vertical increase in yield in the spectra and is the point at which the RBS spectrum first shows the presence of an element in the sample. Back-scattering does not occur from the element at energies above the point of this leading edge.[2] The yield at energies lower than this leading edge result from back-scattering from other atoms in the sample.

The sample whose spectrum is shown in Figure 1, SiO_2, is not monatomic. To understand how the different ele-

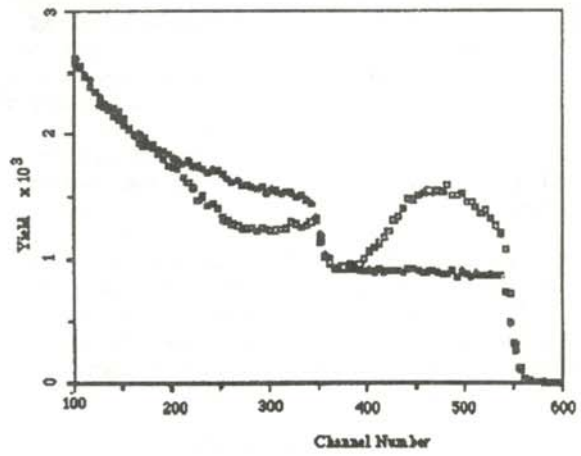

Figure 1
2 MeV Rutherford back scattering spectra for unimplanted SiO_2 (solid boxes) and SiO_2 implanted with Si (open boxes).

Ken Jensen recently acquired a B.Sc. in Engineering Physics. This work is a summary of the project required for the awarding of that degree. The author is presently a Project Engineer at Copeland Corporation, doing finite element analysis.

ments effect the spectra, one has the following rules:

1) Heavier masses have a leading edge at higher energies due to the kinematics of two body scattering [3]
2) High atomic numbers give high yield due to the dependence of scattering cross-section on the atomic number.

These effects can be seen in Figure 1 by looking at the un-implanted sample (data indicated by the solid circles). Since Si is more massive than O, the leading edge for Si is at channel 550 while that for O is at channel 350. If the yield between channel numbers 400 and 500 is extrapolated back to channel 100, all counts below that line are due to back-scattering from Si deep inside the sample. The counts between channel 100 and 350 that lie above the extrapolated line are due to back-scattering from oxygen.

The open square data are for a sample of SiO_2 which was implanted with 8×10^{17} Si atoms per cm^2 at 135 keV. This causes a compositionally non-uniform sample in the depth profile. Since the sample's atomic concentration is non-uniform in depth, the energy loss per unit depth is also non-uniform, causing a varying depth per channel relationship (the energy loss is proportional to channel number). This effect can be observed by noticing the 'hump' in the implanted sample between channels 400 and 500. This 'hump' is due to an increased concentration of Si atoms at this depth. These additional atoms cause the energy loss to change from what it would be if the extra atoms were not present. The additional Si atoms also cause the yield from oxygen in the implanted sample to have a small yield value between channel 250 and 300. This non-uniform energy loss has caused a problem in analyzing the concentration as a function of depth in this type of sample.

We have developed a fast, simple method for analyzing such spectra. First, a procedure was developed to calculate the atomic fractions and stoichiometry directly from the RBS spectrum. Second, some physically reasonable assumptions are made about the concentration relationship of the atoms (Si and O). Using these assumptions, one can deduce a depth distribution and volume concentration for the implanted atoms (Si). Once the analysis is completed for the Si part of the yield, one can repeat the procedure for the oxygen part of the yield from the RBS spectrum. If the assumptions make are physically correct, the concentration as a function of depth should be identical for the two parts. We found that two such assumptions do indeed result in self-consistent depth distributions for the implanted Si, but that the depth distributions are no unique.

THEORY

The sample was divided into its two constituents: the subscript 'a' refers to the Si and subscript 'b' to the oxygen. We further divided the sample into layers parallel to the sample surface. The yield of the back-scattering spectrum from element 'a' in a layer with index 'i' was expressed as:[4]

$$A_{ai} = \frac{\sigma_a \, \Omega \, \Delta E_{ai} \, f_{ai}}{\cos\theta_1 \, [\varepsilon_a^{ab}]_i} \quad , \tag{1}$$

where σ_a is the Rutherford scattering cross-section for scattering from element 'a', Ω is the solid angle subtended by the detector, Q is the number of particles incident on the sample, θ_1 is the angle between the sample normal and the incident trajectory, ΔE_{ai} is the energy interval corresponding to particles back-scattered from element 'a' in layer 'i', f_{ai} is the atomic fraction of element 'a' in layer 'i' and $[\varepsilon_a^{ab}]_i$ is the stopping cross-section fraction for an ion passing through a mixture of elements 'a' and 'b' which scatters from element 'a' in layer 'i'. The kinematic factor, K, affects the yield only through the stopping cross-section factor (see Equation 2). Equation 1 is specifically written for yield from atoms of type 'a'. Those variables having a subscript 'a' will take on different values if the yield from atoms of type 'b' are considered.

The stopping cross-section factor gives the energy lost to electrons weighted by the number of atoms in the target which an incident ion encounters. This is a function of the energy of each particle and the geometry of the path taken. The surface energy approximation assumes that this loss rate is constant with each of the in-going and out-going paths. Ignoring the layer designation, this is expressed as:[5]

$$[\varepsilon_a^{ab}] = \frac{K_a \, \varepsilon^{ab}(E_o)}{\cos\theta_1} + \frac{\varepsilon^{ab}(K_a E_o)}{\cos\theta_2} \quad , \tag{2}$$

where K_a is the ratio of the energy ion before and after a collision with an atom of type 'a', $\varepsilon^{ab}(E)$ is the stopping cross-section for an ion moving with energy E through a material made up of 'a' and 'b' atoms. θ_2 is the angle between the sample surface normal and the back-scattering trajectory.

The Bragg rule [6] says that stopping cross-sections for mixtures can be found from elemental stopping cross-sections by:

$$\begin{aligned} \varepsilon^{ab}(E_o)_i &= f_{ai} \, \varepsilon^a(E_o) + f_{bi} \, \varepsilon^b(E_o) \\ \varepsilon^{ab}(K_a E_o) &= f_{ai} \, \varepsilon^a(K_a E_o) + f_{bi} \, \varepsilon^b(K_a E_o) \quad , \end{aligned} \tag{3}$$

Combining equations 2 and 3 yield:

$$[\varepsilon_a^{ab}] = f_{ai} \, [\varepsilon_a^a] + f_{bi} \, [\varepsilon_a^b] \quad , \tag{4}$$

where

$$\begin{aligned} [\varepsilon_a^a] &= \frac{K_a \, \varepsilon^a(E_o)}{\cos\theta_1} + \frac{\varepsilon^a(K_a E_o)}{\cos\theta_2} \\ [\varepsilon_a^b] &= \frac{K_a \, \varepsilon^b(E_o)}{\cos\theta_1} + \frac{\varepsilon^b(K_a E_o)}{\cos\theta_2} \quad . \end{aligned} \tag{5}$$

Equation 5 may be interpreted as the stopping cross-section factor of the respective element. These values are independent of the depth at which the scattering occurred and of the local composition. They do depend on the fact that they were scattered from an atom of element 'a'.

Equation 5, on the other hand, shows directly the variation in stopping power caused by varying the composition.

Substitution Equation 3 into Equation 1 gives an expression for the yield:

$$A_{ai} = \frac{\sigma_\alpha \, \Omega \, \Delta E_{ai}}{\cos\theta_1 \, [\varepsilon_a^a + S_i(\varepsilon_a^b)]} \quad , \qquad (6)$$

where Si is the stoichiometry, (see Equation 8).

This expression contains parameters that are readily extractable from the RBS spectra except for the stoichiometry. The stoichiometry can then be found by rearranging Equation 6:

$$S_i = \frac{\sigma_a \, \Omega \, \Delta E_{ai} - A_{ai} \, \varepsilon_a^a \cos\theta_1}{\cos\theta_1 \, A_{ai} \, \varepsilon_a^b} \quad . \qquad (7)$$

The stoichiometry is obtained by comparing the spectra of an un-implanted sample with known stoichiometry and the spectra of an implanted sample. In that case, σ_a,Ω, ΔE_{ai} and $\cos\theta_1$ divide out since they are the same for both spectra. Once the stoichiometry for each channel has been calculated, the atomic fractions are found by:

$$S_i = \frac{f_{bi}}{f_{ai}} \qquad (8)$$

$$1 = f_{ai} + f_{bi} \quad .$$

The energy width of a layer is given by:

$$\Delta E_{ai} = [\varepsilon_a^{ab}]_i \, N_{si} = [\varepsilon_a^{ab}]_i \; N_{vi} \, t_i \quad . \qquad (9)$$

where N_{si} is the total number of atoms per cm^2 for each layer, N_{vi} is the volume concentrations in a layer 'i' whose thickness is t_i.

The stopping cross-section factor for each layer can be calculated from Equation 3 using the atomic fraction deduced from Equations 8. The stopping cross-sections factors then can be used along with Equation 9 to find N_{si}.[7] By making some reasonable assumptions about the atomic densities in an inhomogeneous target, such as that shown in Figure 1, we can infer the concentration of the element of interest in the sample and the depth at which this concentration lies. Such assumptions might include: a) that the atomic concentration of oxygen in implanted SiO_2 remains constant, or b) the total number of atoms/volume remains constant. If assumptions about the concentration can not be made, the RBS spectrum can be broken up into energy intervals having the same number of atoms per cm^2. These intervals are not of a fixed thickness. Since most materials are made of of atoms that are nearly close packed, the thickness intervals will be within a factor of 2.

ANALYSIS OF RESULTS

Figures 2 shows the stoichiometry as derived from the Si and oxygen portions of the spectrum shown in Figure 1. The trend of the stoichiometry is the same, even though the scaling is different. This indicates that the procedure used to deduce the stoichiometry does not depend on which constituent of an inhomogeneous sample is used in the analysis.

Figures 3 and 4 show that the stoichiometry of the sample is independent of the assumptions made about the atomic concentration. Figures 3 shows the concentration as a function of depth. The volume concentration vs. depth is independent of whether the Si or oxygen portion of the spectrum is used. This based on the assumption that the oxygen concentration was unaffected by the implantation of the Si.

Figure 4 shows the volume concentration vs depth deduced from the back-scattered yield from Si atoms. These results are based on the assumption that the total number of atoms in a given volume is constant.

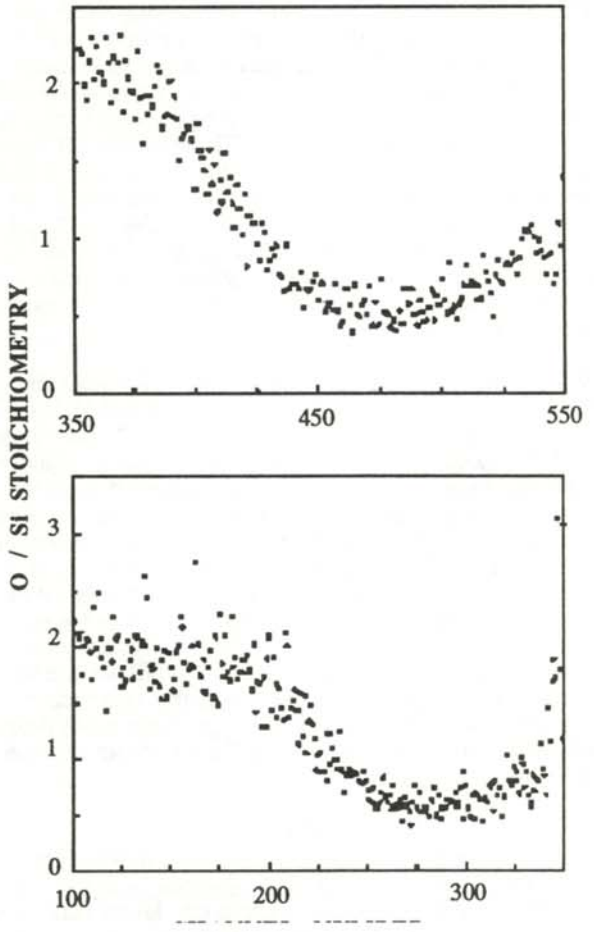

Figure 2
The oxygen/silicon stoichiometry vs channel number for SiO_2 deduced from the back scattered yield. The top graph, where sample surface is located at channel 550, is the yield from Si atoms. The lower graph is deduced from the yield of oxygen atoms. The sample surface is located at channel 340.

The results indicated that the assumptions we made about the concentrations are self consistent. When the results of our assumptions are compared to results derived from Monte-Carlo type methods[8], we found some inconsistencies.

Comparison of the concentration vs depth curves deducted from either the oxygen or silicon RBS yields in Figure 3 or a similar comparison in Figure 5 show that the results for a given assumption about the density to be consistent. This justifies the internal reliability of the procedure to give the proper trends in the data. Comparison of the yields for the different assumptions about density (Figure 3-top and Figure 4-top), however, show that the maxima occur at different depths, that the range of the implanted ions are different and that the absolute values of the concentration differ.

This indicates that the procedure will work with any arbitrary assumption made about the atomic densities and that the concentration is numerically very sensitive to the

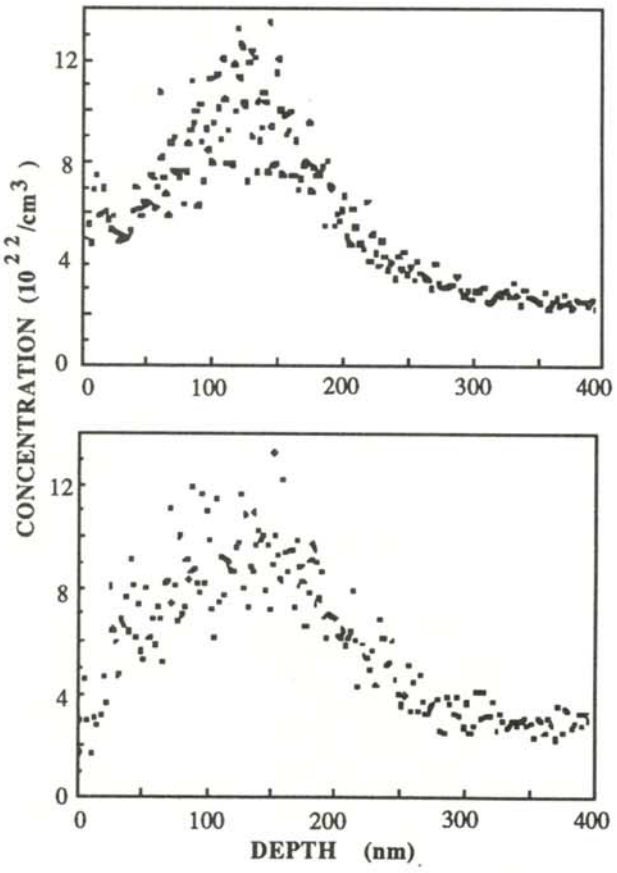

Figure 3
Volume concentration of Si vs. depth in the implanted SiO2 sample deduced from back scattering. The top figure is the concentration deduced from back scattered yield from Si atoms and the bottom figure from the back scattered yield from oxygen atoms. These results are based on the assumption that the implantation did not affect the oxygen distribution.

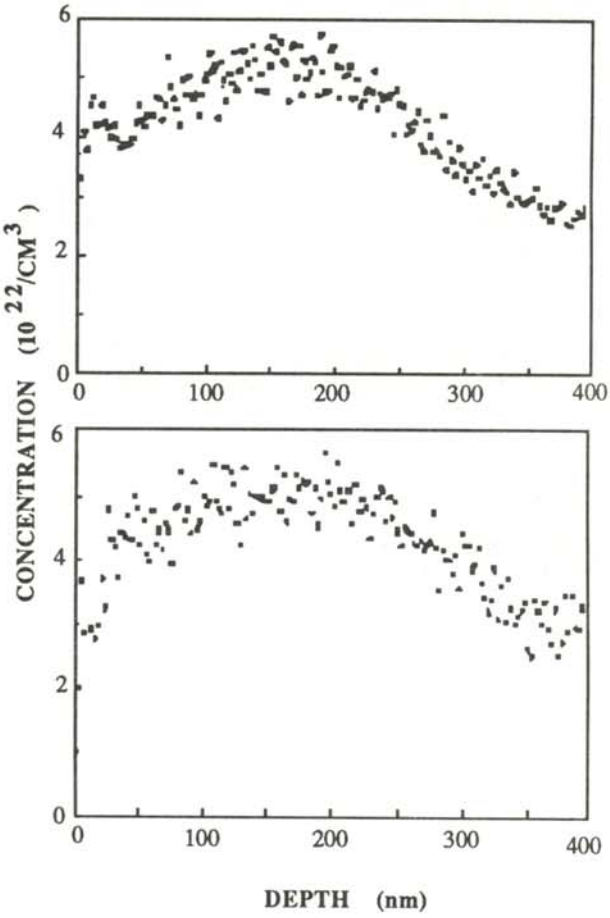

Figure 4
Volume concentration of Si vs. depth in the implanted SiO_2 sample deduced from the back scattered yield . The top graph is the concentration deduced from the yield from Si atoms and the bottom graph from the yield of oxygen atoms. The results are based on the assumption that the total number of atoms per depth stayed constant,

assumption made about atomic density. It be necessary to find a way to make reliable determinations about densities to be able to use the procedure to extract concentration-depth profiles with numerical accuracy.

ACKNOWLEDGMENTS

A special thanks to Dr. Gary Farlow for his leadership and guidance. He also provided the RBS spectra that were used in the analysis.

REFERENCES

* Current address of author: Copeland Corporation, 1675 West Campbell Road, Sidney, OH 45365-0669.

1. W.K. Chu, J.W. Mayer, M.A. Nicolet, Backscattering Spectroscopy, Academic Press, New York, 1978, p. 14.

2. Ibid., p. 16.

3. Ibid., p. 16.

4. Ibid., p. 82.

5. Ibid.. p. 62.

6. W.H. Bragg, R. Kleeman, Phil. Mag. 10, 1905, p. S318.

7. W.K. Chu, op.cit. p. 74.

8. J.F. Ziegler, J.P. Biersack, U. Littmark, The Stopping and Range of Ions in Solids, Pergamon Press.

FACULTY SPONSOR

Dr. Gary Farlow
Physics Department
Wright State University
Dayton, OH 45435

Transient Energy Transfer in ZnSe

Perry P. Beissel †
Thomas B. Rossman †
Christopher J. Watrud †
Department of Physics
United States Military Academy
West Point, NY 10996
received August 23, 1991

ABSTRACT

Energy transfer between two optical pulses overlapping in time and space inside a ZnSe sample was investigated. A mode-locked, Nd:YAG laser provided high intensity pump and low intensity probe beams. Changes in gain in the probe were observed as the input intensity and relative arrival times of the pump and probe beams were varied. Accurate analysis was facilitated by careful characterization of the laser output. A numerical model of the energy transfer process was developed based on the Transient Energy Transfer theory. This model, implemented using a personal computer, compared favorably to the experimental results.

INTRODUCTION

Two optical beams crossing in a nonlinear medium produce an interference pattern that can induce a refractive index grating. Energy can be transferred from the stronger to weaker beam if there is a shift between the phase of the interference pattern and the index grating.[1] The shift may result from a non-local effect, such as in photo-refractive materials,[1,2] or from a local effect if the intensity of the incoming beams varies in time.[1]

In poly-crystalline ZnSe, the photo-refractive effect does not produce net energy transfer because of the random orientation of the crystallites. However, if short pulses are used, a transient index grating can be produced by the generation of free charge carriers that transfer energy between the pulses. This mechanism is known as Transient Energy Transfer (TET).

To explore this effect in ZnSe (a wide gap II-VI semiconductor), a pump-probe experiment was conducted using a 10 Hz mode-locked Nd:YAG laser with frequency doubling which produced 25 ps pulses at 532 nm. Individual pulses were optically separated into an intense pump, a weak probe and a sampling beam. The relative arrival time of the pump and probe at the crystal and the intensity of the pump were varied.

The TET theory was implemented on a personal computer using a fourth order Runge-Kutta numerical scheme. The numerical results were compared with experimentally obtained data in order to determine the viability of the model.

Perry Beissel, Tom Rossman and Chris Watrud graduated from the United States Military Academy in June 1991 with Bachelors of Science in Engineering Physics and are now serving as Second Lieutenants in the army. They performed this work jointly as part of an advanced independent research project.

THEORY

The energy transferred from a strong pump to a weaker probe was modeled using the TET theory,[1,3,4] in which the free carrier generation mechanism is two-photon absorption (TPA). Two light pulses of wavelength λ crossing with an angle 2θ develop a transverse intensity interference pattern whose spatial period Λ (See Figure 1) is given by the equation:[5]

$$\Lambda = \frac{\lambda}{2 \sin\theta} \,. \qquad (1)$$

Inside the semiconductor, the intensity interference pattern generates a matching pattern of free electrons and holes through the TPA process. In turn, the spatially varying free carrier population produces a variation in index of refraction through the Drude-Lorentz model,[6] resulting in an index of refraction (phase) grating that extends into the medium.

Each beam experiences diffraction as it passes through the phase grating, scattering light into several diffraction orders on either side of its incident direction (zeroeth order). Because the phase grating is written by the two beams, the geometry of the situation guarantees each will diffract some light (in first order) into the other. Light diffracted into the first order suffers a 90 degree phase shift with respect to the zeroeth order.[3] Therefore, as the two beams propagate through the medium, they accumulate phase-shifted light that changes their net phases (but not necessarily their amplitudes).

If the input beams are of unequal intensity, a net phase difference between pump and probe beams develops with

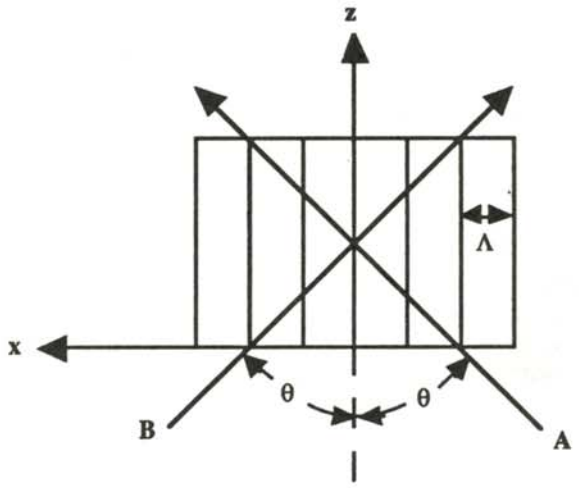

Figure 1
Interference pattern of two coherent beams of light crossing in a medium at an angle 2θ. The period of the intensity pattern Λ is related to the crossing angle and wavelength of light according to Equation 1. A matching pattern of free carriers will be generated through two photon absorption.

propagation distance in the crystal. As a result, the interference pattern shifts transversly in phase (toward the weaker beam) as the beams move deeper into the crystal. If recombination of the free carriers in the semiconductor is instantaneous, the phase grating will keep pace with the shifting interference pattern and no net energy transfer occurs. However, if there is a finite recombination time, the phase grating will lag the interference pattern. The phase lag between the interference pattern and the phase grating results in energy transfer from the strong to weak beam. The greatest energy transfer occurs for a phase difference of 90°.[7]

The evolution of similarly polarized beams crossing in ZnSe is modeled by the following first order differential equations. These are derived by application of the slowly varying envelope approximation to the wave equation with sources that include third order nonlinearities in the fields (two photon absorption, nonlinear refraction) and interaction with the free carriers:[8]

$$\cos\theta \frac{d}{dz}A^2 = -2\gamma_1 N_2 A B \sin(\phi - \nu) - [\alpha + \beta_2(A^2 + 2B^2) + \sigma_{eh} N_o] A^2$$

$$\cos\theta \frac{d}{dz}B^2 = +2\gamma_1 N_2 A B \sin(\phi - \nu) - [\alpha + \beta_2(2A^2 + B^2) + \sigma_{eh} N_o] B^2 \qquad (2)$$

$$\cos\theta \frac{d\phi}{dz} = \gamma_1 N_2 \left(\frac{A}{B} - \frac{B}{A}\right) \cos(\phi - \nu) - \beta_1 (A^2 - B^2) .$$

A and B are the amplitudes of pump and probe beams, $\phi = \phi_B - \phi_A$ is the difference in phase between probe and pump, and z measures the depth in the crystal along the bisector of the two beams. N_0 and N_2 are the Fourier components of free carrier densities as described in the next paragraph. The constants found in these equations and others are given in Table 1.

The free carrier concentration is most conveniently described in terms of a "DC" background level N_0 and a modulation N_2 of period Λ and phase ν:

$$N = N_o + 2 N_2 \cos\left(2\pi \frac{x}{\Lambda} + \nu\right) . \qquad (3)$$

The x coordinate measures transverse position in the crystal. The free carrier concentration will evolve according to:[8]

$$\frac{\partial N_o}{\partial t} = \frac{\beta_2}{2\hbar\omega} [(A^2 + B^2)^2 + 2A^2 B^2] - K_2(N_o^2 + 2N_2^2)$$

$$\frac{\partial N_2}{\partial t} = \frac{\beta_2}{\hbar\omega} (A^2 + B^2) A B \cos(\phi - \nu) - 2 K_2 N_o N_2 \qquad (4)$$

$$\frac{\partial \nu}{\partial t} = \frac{\beta_2}{N_2 \hbar\omega} (A^2 + B^2) A B \sin(\phi - \nu) .$$

The pulses of light were taken to be Gaussian in time:

$$A = A_o \exp\left[-4 \ln 2 \frac{t^2}{\tau_p^2}\right] ,$$

$$B = B_o \exp\left[-4 \ln 2 \frac{(t - \Delta t)^2}{\tau_p^2}\right] , \qquad (5)$$

where Δt is the time delay between pump and probe, and τ_p is the pulse length (FWHM).

The system of six coupled differential equations given by Equation 2 and Equation 4 were solved self-consistently using a fourth-order Runge-Kutta scheme implemented in

Turbo Pascal on a personal computer. The pulses were sliced into time steps which were numerically propagated through the 3.0 mm depth of the ZnSe sample used. The code was designed so that the pump and probe intensities, the delay between pump and probe, and the integration step sizes (time and space) were adjustable. Stabilization of probe gain was used to signal convergence of the code as time and space steps were made smaller. The results of the experimental beam characterization were applied to determine peak intensities of pump and probe and pulse width, and the values of the material constants from Table 1 were utilized. The parameters β_1 and K_2 are not well known for this material, so they were treated as adjustable constants to bring the magnitude of the probe gain at optimal delay into agreement with experimental results.

EXPERIMENT

The experimental setup is shown in Figure 2. The Nd:YAG laser output, at 10 Hz, is frequency doubled to 532 nm with an output energy of 35 mJ. The beam, after passing through a series of fixed and variable attenuators, is split into sample, pump and probe beams. Energies of these beams were measured by energy meters (D1 through D3, respectively) and recorded by a computer through a GPIB interface. By removing the ZnSe sample, the input energies of the pump and probe beams were calibrated against the sampling detector. The probe delay was controlled by the position of a retroreflector (RTR) mounted on a movable stage with position resolution of 10 μm (0.066 ps in arrival time).

It is necessary for the pump and probe to overlap in time and space for the energy transfer process to occur. Analysis and alignment is simplified by using a spatially broad and smooth pump, a relatively small probe, and a small crossing angle between the beams. A 500 mm lens focused the probe to a spot size of 0.125 mm and the condensing doublet followed by a 1000 mm lens focused the pump to a spot size of 0.75 mm. The crossing angle is 12.5°, which corresponds to an angle of 4.7° inside the sample due to its high index of refraction.

Neutral density filters controlled the incident energies. A pump intensity of 1-2 GW/cm^2 is sufficient for measurable energy transfer to occur.

Ref.	Material Constant	Value
9	Index of refraction (n_o)	2.7
10	Attenuation coefficient α	0.6 cm^{-1}
11	Nonlinear ref. coeff (β_1)	10 cm/GW
12	TPA coefficient (β_2)	5.5 cm/GW
13	"Drude" ref. coeff (γ_1)	1.6x10^{-16} cm^2
14	Free carrier cross-sec(σ_{eh})	2x10^{-18} cm^2
15	Recombination rate (K_2)	5x10^{-8} cm^3/s

Table 1

Constants used in modeling Transient Energy Transfer in ZnSe. Uncertainties are implied by the least significant figure, except for K_2 which has a larger uncertainty (see reference).

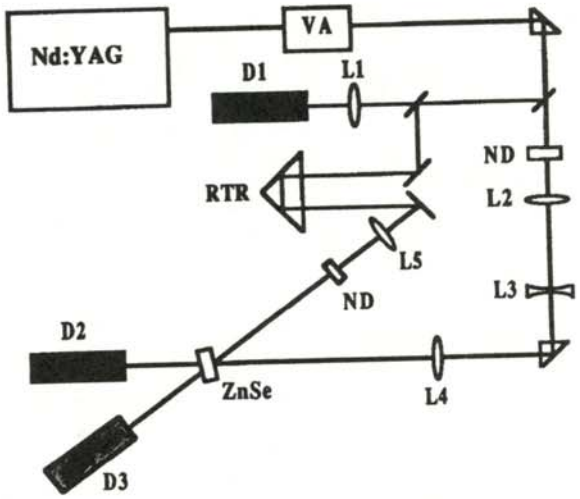

Figure 2

Pulses of 532 nm light produced by the Nd:YAG laser are split into three beams. The sampling detector (D1) measures incident energy on a pulse-by-pulse basis. Detectors D2 and D3 measure pump and probe throughput energies. A retroreflector (RTR) mounted on a translation stage controls probe arrival time. ND: high power neutral density filters; L1-L5: fused silica lenses; VA: variable attenuator.

A Big Sky Multicam™ system was employed to determine the spot size and spatial profile of the two beams. This system was used to facilitate the adjustments to the optical elements needed to attain the desired spot sizes stated above. The camera system also verified the Gaussian shape of the beam's spatial profile at the crystal.

The nominal temporal pulse width of the frequency-doubled beam is about 25 ps based on estimates derived from the manufacturer's specifications. It was actually measured using two methods. The first method employed a single-pulse autocorrelator which encodes the temporal extent of a pulse along one spatial dimension. Using this instrument we measured the pulse width to be $\tau_p = (23 \pm 2)$ ps with negligible pulse to pulse variations. The uncertainty arises from estimating the FWHM of a reticon readout on a CRT storage oscilloscope.

The second method utilized the known nonlinear transmission characteristics of ZnSe to calculate the pulse width. This method assumes that the dominant nonlinear attenuation mechanism of an intense pulse of light in ZnSe is due to two-photon absorption (TPA), according to the equation:[12]

$$\frac{dI}{dz} = -\alpha I - \beta_2 I^2 \ . \qquad (6)$$

If the pulse is Gaussian in space and time:

$$I = I_o \exp\left[-2\frac{r^2}{\omega^2} \right] \exp\left[-8 \ln 2 \frac{t^2}{\tau_p^2} \right] , \qquad (7)$$

with spot size ω and pulse width (FWHM) τ_p, then the energy transmission E_{out}/E_{in} can be computed from Equation 6 by integration in space and time. Using the values of α and β_2 from Table 1 and a calculated reflectivity of R = 0.21 at both front and back surfaces, we computed the curve shown as a solid line in Figure 3. This curve depicts the inverse transmission (E_{in}/E_{out}) as a function of **peak** intensity. Note the curve makes no assumptions about the values of ω or τ_p; these cancel out of the calculation. Only the Gaussian forms are assumed.

The inverse transmission 1/T for a series of nearly equal pump pulses (input energy E_{in}) was measured and placed on Figure 3 (shown as open squares). The vertical placement is fixed, while the horizontal placement was adjusted to give the best agreement between data and the curve. From this placement we deduce the peak input intensity I_o, related to input energy by:

$$I_o = \frac{2\,E_{in}}{\pi\,\omega^2}\,\frac{1}{1.06\,\tau_p}\,, \qquad (8)$$

which follows from the Gaussian forms assumed. Since the pump spot size ω is directly measured the only unknown is the pulse width τ_p. The determination of the pulse width utilizing nonlinear transmission characteristics of ZnSe yielded a value of $\tau_p = (24.5 \pm 2)$ ps. We employ a value of $\tau_p = 24$ ps for analysis.

Twenty pulses were fired at each delay and attenuator setting during the course of the experiment. For each shot the sampled energy (and through calibration, the input energy), pump throughput energy, probe throughput energy, and delay stage setting were recorded. Probe throughput was recorded periodically with the pump blocked to establish a baseline for gain calculation. Pulses were manually triggered at about five second intervals.

Two studies were performed. First, with a fixed pump energy level (establishing a nominal incident intensity of about 1 GW/cm^2), data was recorded at delay times spanning 90 ps, centered roughly on the point of maximum gain. Second, with the delay set at peak gain, pump energy was adjusted using the variable attenuator.

RESULTS

The results of our first gain study are shown in Figure 4. For each delay setting, the twenty data sets were refined by rejecting input pulses that fell outside a window of about ±5% in energy, with a center energy of about 300 μJ for the input pump pulse. This translates to a peak pump intensity of 1.25 GW/cm^2. Typically half the pulses fell inside the window. The gain of each probe pulse fired with the pump present was calculated with respect to the probe throughput with pump blocked. The mean and standard deviation of the probe gain at each delay setting are plotted in Figure 3. Negative delay times correspond to arrival of the probe after the pump.

As expected, at delays corresponding to widely separated pump and probe arrival times (>50 ps from the point of peak gain), there was no effective interaction between the two and a gain of unity was observed. A peak gain of 3.7± 0.6 was observed, and this delay setting is taken as the arbitrary zero delay point. The gain fell steeply on either side of this point, with a FWHM of about 15 ps. An interesting effect was seen at delay settings of -15 to -40 ps in that the gain was actually less than unity. This is to be expected if enough free carriers remained in the sample to cause attenuation of the probe.

The code developed was run through a scan of probe delay settings in order to obtain a theoretical gain curve. This scan resulted in a curve with the same basic shape as the experimental data, having a large peak and a region of absorption on one side, as shown in Figure 5. The essential difference between the code plot and experimental data plot is the width of the gain peak. The values of β_1 and K_2 that gave the best match of the peak gain and maximum absorption to the data were:

$$\beta_1\text{: } 10 \text{ cm/GW}, \qquad K_2\text{: } 3.6 \times 10^{-8} \text{ cm}^3/\text{s}.$$

Note that the code predicts peak gain will occur when the probe pulse arrives about 10 ps before the pump pulse. With a suitable diagnostic (such as a streak camera) this prediction could be tested.

In the second part of the experiment, the delay was set to nominal zero and gain was measured as the pump intensi-

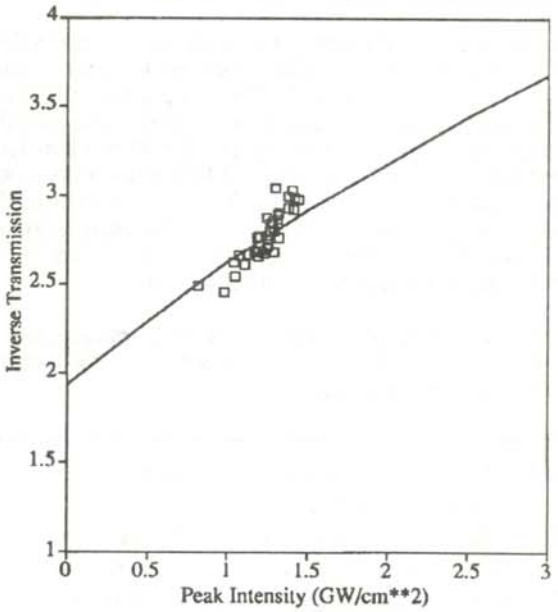

Figure 3
Inverse transmission curve for 532 nm pulses passing through ZnSe. Solid curve is a calculation based on propagation of a Gaussian pulse through a 3mm deep sample of CVD ZnSe. Free carrier absorption is not included. Solid squares are measured inverse transmission values. Horizontal placement of the data on the curve requires a pulse width of about 24 ps (FWHM) through equation (8).

ty was varied by adjusting the variable attenuator. For each attenuator setting, the twenty data sets were refined as described above, and using the remaining data the means and standard deviations of the gains were again calculated and plotted against the calculated input intensity. The results of this investigation are shown in Figure 6. As expected, the gain climbs rapidly as peak pump intensity is increased.

The code was also used to perform a study of probe gain versus pump intensity. The delay was set for maximum gain (as in the experiment) and the pump intensity was varied. The result is shown as the solid curve in Figure 6. Note the code predicts both greater absorption and greater gain than observed.

SUMMARY

Under the proper conditions, energy transfer occurs between pump and probe beams interacting in ZnSe, a wide gap II-VI semiconductor. Gain in the probe beam varies with pump intensity and relative arrival time between pump and probe. Reasonably good agreement between the code results and the data provide support for modeling the beam coupling interaction with the transient energy transfer theory. In particular, the values of β_1 and K_2 that gave the best match in peak gain and absorption as a function of probe delay were quite reasonable. However, deviations between the data and the theory are significant enough to cause us to re-examine the assumptions. In particular, the difference in the width of the gain curves in Figures 4 and 5 and the mismatch in gain at lower and higher peak pump intensities (Fig. 6) indicate the presence of some systematic error. One possible source is the unverified assumption that the pulses were Gaussian in time. Another is the assumption in the code that the two pulses are fully coherent. Future work with both

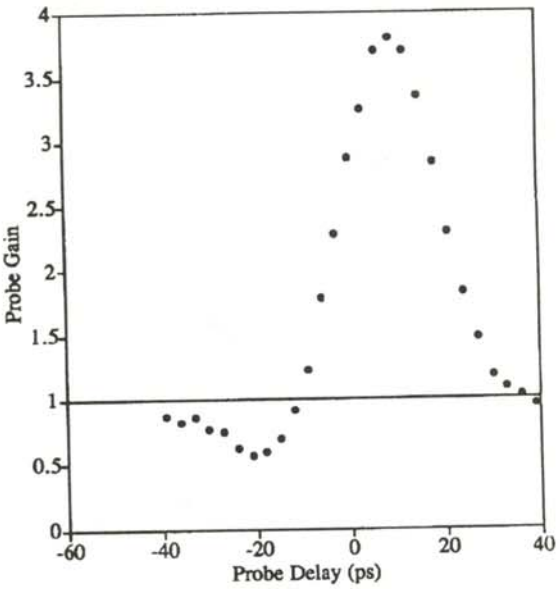

Figure 5
Theoretical probe gain as a function of delay between arrival of pump and probe in ZnSe. Negative delay corresponds to probe arriving after pump. Appropriate experimental parameters were used in performing the calculations.

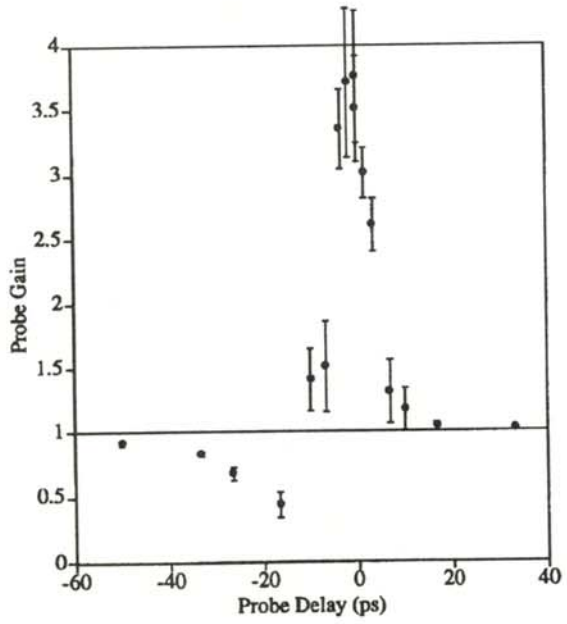

Figure 4
Experimental probe gain as a function of delay between arrival of pump and probe in ZnSe. Negative delay corresponds to probe arriving after pump. The zero is arbitrarily set at peak gain. Peak pump intensity is approximately 1.25 GW/cm^2

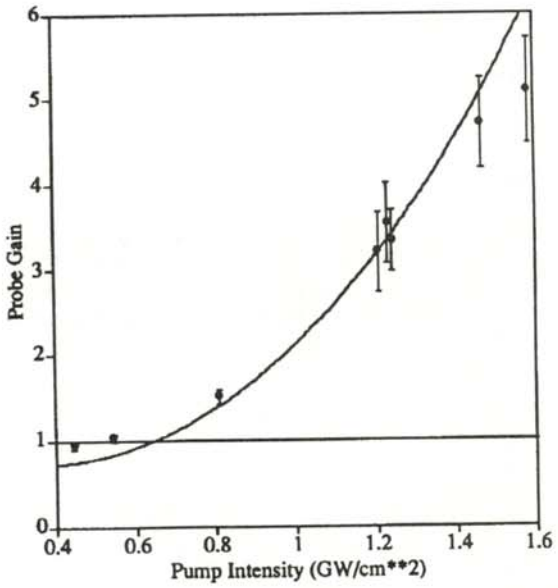

Figure 6
Probe gain as a function of peak pump intensity. The solid curve is predicted by the Transient Energy Transfer theory. Data are indicated with markers and error bars. Delay between arrival of pump and probe has been set for maximum gain in both experiment and theory.

code and diagnostics will examine these possibilities.

ACKNOWLEDGEMENTS

The authors would like to thank LTC John E. La Sala for his direction and sponsorship of this paper, and MAJ Steven S. Cotariu for his valuable assistance. The authors would also like to thank the U.S. Army Research Office and the Photonics Research Center at USMA for making this work possible.

REFERENCES

† Mailing c/o LTC John E. LaSala, Department of Physics, USMA, West Point, NY 10996.

1. V. L. Vinetskii, N. V. Kukhtarev, E. N. Sal'kova and L. G. Sukhoverkhova, Sov. J. Quantum Electron., 10, 684 (1980).

2. J. Feinberg, D. Heiman, A. R. Tanguay, Jr. and R. W. Hellwarth, J. Appl. Phys. 51, 1297 (1980).

3. V. L. Vinetskii, N. V. Kukhtarev and M. S. Soskin, Sov. J. Quantum Electron., 7, 230 (1977).

4. G. C. Valley and A. L. Smirl, IEEE J. Quantum Electron., QE-21, 488 (1985).

5. See for example J. Feinberg in Optical Phase Conjugation, R. A. Fischer, ed., Academic Press, NY, 1983, p.421.

6. See for example N. W. Ashcroft and N. D. Mermin, Solid State Physics, Holt, Reinhart and Winston, NY, 1976, Ch.1.

7. D. W. Vahey, J. Appl. Phys., 46, 3610 (1975).

8. Adapted from Ref. 4.

9. Two-Six Inc., Saxonburg, PA 16056.

10. Measured.

11. Related to the nonlinear refractive index n_2 by $\beta_1 = (\omega/c)\gamma$, where $\gamma(m^2/W) = (40\pi/cn)n_2(esu)$. Value of n_2 used is taken to be twice that of CdS based on an empirical relationship from N. L. Boling, A. J. Glass and A. Owyoung, IEEE J. Quantum Electron., QE-14, 601 (1978).

12. E. W. Van Stryland, et. al., Opt. Engr., 24, 613 (1985).

13. Calculation based on R. K. Jain and M. B. Klein in Optical Phase Conjugation, R. A. Fischer, ed., Academic Press, NY, 1983, p.335.

14. Calculation based on Ref. 6 and mobility and effective mass data from M. A. Omar, Elementary Solid State Physics: Principles and Applications, Addison-Wesley, NY, 1976, Ch.6.

15. Measured; uncertainty +100% -50%.

FACULTY SPONSORS

LTC John E. La Sala
and
MAJ Steven S. Cotariu
Department of Physics
United States Military Academy
West Point, NY 10996

VIDEO RECORDING TECHNIQUES AND LARGE-ANGLE PENDULUM MOTION†

John Slotwinski*
Department of Physics
Loyola College
Baltimore, MD 21210
received 8/13/91

ABSTRACT

Video-recording techniques were used to record the motion of a simple undamped pendulum with large-angle displacements and determine the trajectory of the pendulum bob. A comparison was made with numerical solutions to the problem. There was good agreement between theoretical and experimental results.

INTRODUCTION

The pendulum system is one topic that all students of physics study at one time or another. Generally it is used to illustrate simple harmonic motion. The mathematical analysis that is typically done in freshman physics is a linear approximation to the real motion. It only holds true for small angle displacements of the pendulum. The description of large-angle displacements require solutions to a non-linear second-order differential equation.

$$\frac{d^2\theta}{dt^2} = -\frac{g}{L}\sin\theta\,, \tag{1}$$

where θ is the displacement angle of the pendulum from vertical, L is the length of the pendulum and g the acceleration due to gravity. The solution for this case where the angle θ is not « 1 radian gives a period that can be approximated as:

$$T = 4\sqrt{\frac{L}{g}}\,\frac{\pi}{2}\left\{1+\left(\frac{1}{2}\right)^2\sin^2\left(\frac{\alpha}{2}\right) + \left(\frac{1\cdot3}{2\cdot4}\right)^2\sin^4\left(\frac{\alpha}{2}\right)\ldots\right\}, \tag{2}$$

where α is the maximum displacement angle. This shows that the period is dependent upon the amplitude of the motion.

The motion of a pendulum with large angular displacements has been recorded using a helipot[1] and stroboscopic photography [2]. In this paper, we use video-recording techniques to study the large-angle undamped pendulum motion. These techniques, while fairly new, have been used in other contexts. For example, the rise of carbon dioxide bubbles in a glass of beer have been monitored using this technique.[3] Because of technological improvements and reductions in cost, video cassette recorders and video cameras are now practical tools in the undergraduate laboratory.

THE EXPERIMENT

The motion of a simple pendulum was recorded using a camcorder and a VCR[4]. Data were taken for pendulum lengths of 1 and 0.5 meters with initial displacement angles of 5, 10, 25, 40 and 50 degrees. The smaller angle data were used as a control to insure that the data taking procedure and subsequent comparison with the numerical solutions were behaving as expected.

A protractor mounted behind the pendulum string provided the angle measurements. Several oscillations for each amplitude were recorded. The angular position of the bob during the oscillations was then manually read from the video monitor using the frame advance feature (1/60 sec. increments) of the VCR. The results were entered into a spreadsheet and stored on disk for later use.

RESULTS

The solution to Equation 1 was obtained using a fourth-order Runge-Kutta numerical method.[5] This method calculated the derivative of the function four times for each

John Slotwinski graduated Cum Laude with a B.Sc. in physics from Loyola College (Maryland) in 1991. John is now a teaching assistant at the Catholic University of America, where he is pursuing his Ph.D. in physics. In 1989, he served as SPS Associate Zone Councillor for Zone 4. When not in school, John works for the Ultrasonic Standards Group at The National Institute of Standards and Technology. John, as a senior, did this work as the semester project for Methods of Applied Math II.

time step: once at the beginning point, twice at the midpoint of the step and once at the end of the step. This method is a superior algorithm for solving second order differential equations.[6]

In general, there was good agreement between the theoretical predictions and the experimental data as recorded by the camcorder. Figures 1 - 3 show our experimental data (square points) and the numerical solutions to equation 1 using the Runge Kutta algorithm (line). Reading the data from the video recording resulted in not having each graph starting with the pendulum at rest. The theoretical fit to the data was started with the same initial conditions as those of our data.

Figure 1 is a comparison of the data with a 5° displacement (open data points) and a 25° displacement (solid data points). This graph shows well that the period is (almost) independent of amplitude for small angles. Figure 2 shows what happens to the motion as the amplitude of the motion becomes large. The open data points are for the 5° amplitude motion and the solid data points show the motion for an amplitude of 50°. The lines shown are the numerical solutions to equation 1 with the appropriate amplitudes as initial conditions. Both Figure 1 and Figure 2 show data for a pendulum of length 0.5 m.

Figure 3 is a comparison of the data for a 1.0 meter long pendulum. The open squares are for an amplitude of 10° while the solid data points are for the motion with an amplitude of 50°. The solid line is the numerical solution for the 10° initial condition and the broken line the numerical solution for the 50° initial condition. The correlation between experimental and numerical data is still good, but not as close as in Figures 1 and 2. We believe the discrepancy was due vibrations in the apparatus and

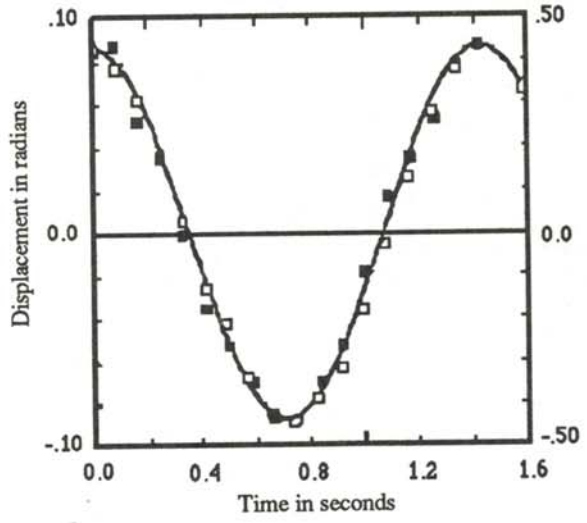

Figure 1
Data for a pendulum of length 0.5 m. The open data points are for an amplitude of 5° (amplitude scale on left) and the solid data points are the motion for an amplitude of 25° (amplitude scale on right). The solid line is a numerical solution to Equation 1.

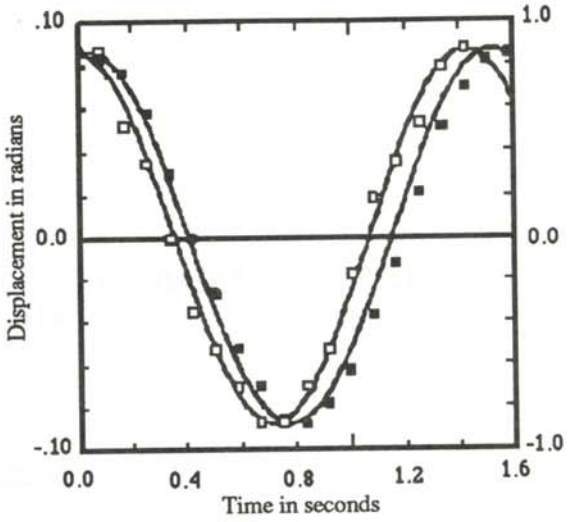

Figure 2
Displacement vs. time for a 0.5 m. long pendulum. The open data points (vertical scale on left) are for an amplitude of 5° and the solid data points (vertical scale on right) are for an amplitude of 50°. The lines are numerical solutions to Equation 1 for the appropriate amplitudes.

uncertainty in the initial conditions of the numerical integration.

Table 1 lists the measured periods for the motion and the

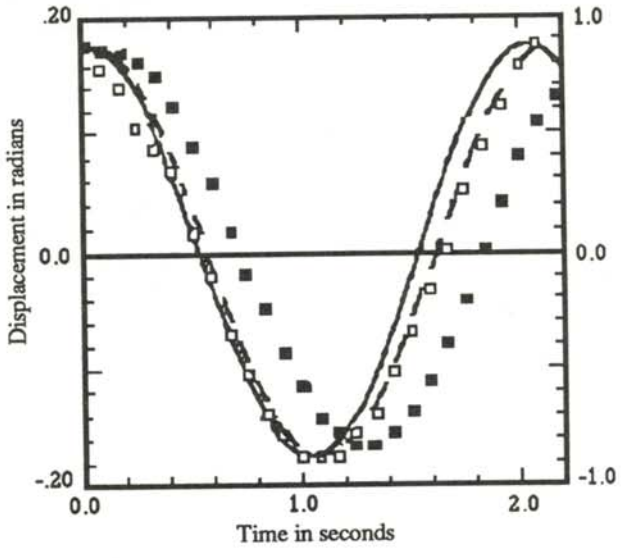

Figure 3
Displacement as a fucntion of time for a 1 m. long pendulum. The open data points (vertical scale on left) are for an amplitude of 10° and the solid points for an amplitude of 50° (vertical scale on right). The solid line is the numerical solution for an initial displacement of 10° and the dashed line for an an initial displacement of 50°.

Displacement (degrees)	Period of the motion experimental (seconds)	theoretical (seconds)
length = 0.5 m		
5	1.42 ± .03	1.42
25	1.42 ± .03	1.44
50	1.58 ± .03	1.52
length = 1.0 m		
10	2.08 ± .03	2.04
50	2.42 ± .03	2.14

Table 1
Measurements of period compared to predictions from Equation 1

values calculated from Equation 2. Once again, there is very good agreement. This equation worked equally well for both lengths of the pendulum.

The generally good correlation between the experimental data and the theoretical solutions make us believe that the video recorded results give a good record of the trajectory of the pendulum. We believe that the video recording method used in this experiment is a reliable method for studying the mechanical system of the pendulum.

ACKNOWLEDGMENTS

The author wishes to thank Howard Moore, Technical Assistant of the Loyola College Department of Physics, for his thoughts, discussions and technical support.

REFERENCES

† Supported by NSF ILI grant No. USE-8951254

* Current address of author: Department of Physics, Hannan Hall, The Catholic University of American, Washington, DC, 20064.

1. S.C. Zilio, Am. Jour. Phys. 50, 1982, pp. 450 - 452.

2. B. Benedict and G. Bruner, Jour. Undergraduate. Res. in Phys., 7, 1989, pp. 31 - 36

3. W. DeZarn and M. Ward, Jour. Undergraduate. Res. in Phys., 7, 1989, pp. 49 - 52.

4. Camcorder, Panasonic Model AG-190-P. VCR, Panasonic Model AG-1730.

5. The Midshipman Differential Equations Program, developed by J.L. Buchanan, a member of the Naval Academy Mathematics Department. Program Version 2.23 was used in this project.

6. W.H. Press, B.P. Flannert, S.A. Teukolsky and W.T. Vetterling, Numerical Recipes, Cambridge University press, 1986, pp. 547 - 554.

FACULTY SPONSOR

Dr. Mary Lowe
Department of Physics
Loyola College
Baltimore, MD 21210

A TEST OF A MONTE-CARLO METHOD FOR DIAGONALIZING HUGE MATRICES †

Randy Blessing
Morningside College
Sioux City, IA 51106
received December 16, 1990

ABSTRACT

An algorithm for approximately diagonalizing huge matrices was tested on some simple examples. The algorithm involves randomly (Monte Carlo) choosing subset matrices of the eigenmatrix, diagonalizing these subset matrices and averaging the results. The results tend to be good for most cases.

INTRODUCTION

Diagonalizing huge eigenmatrices is used in many quantum physics problems. The quantum mechanical interaction energies between electrons form an eigenmatrix which can be diagonalized to yield the electrons' full wave functions. The wave functions then may be used to find position probabilities of the electrons. An eigenmatrix of order 10^{23} could represent the quantum mechanical wave function for all electrons in a rod the size of a small pencil. However, diagonalizing an eigenmatrix of order 10^{23} is a huge problem. It is not possible to exactly diagonalize such an eigenmatrix in a reasonable amount of time even on a very fast computer. The computer that we used on this project would require about 10^{57} years, about 10^{47} times the age of the universe, to do the job.

METHOD FOR DIAGONALIZING

The Monte-Carlo method for diagonalizing a matrix breaks down the 10^{23} order eigenmatrix into something much smaller, such as 1000 x 1000 matrix. The size of these matrices are determined by the limitations of the computer used to do the calculations. These smaller order matrices, called subset matrices, built from the original matrix, are diagonalized and the results averaged together. In this way, the diagonalization of a 10^{23} order eigenmatrix can be approximated using much smaller subset matrices.[1]

Randy is a senior physics and mathematics major at Morningside College. He works part-time off campus as well. After earning his degree, he plans to attend graduate school in mechanical engineering at Iowa State University.

The Monte-Carlo method is used to randomly pick diagonal elements from the original matrix. The off-diagonal elements are chosen from the intersection of two randomly picked diagonal elements. These randomly selected elements are used to build the smaller subset matrices.

There are two conditions an eigenmatrix must meet for this method to work: [2]

1) The off-diagonal elements must be nearly constant,
2) no particular element can greatly deviate from the others.

If these two conditions are not met, the results are poor.

For matrices with nearly constant off-diagonal elements, one eigenvalue lies between each pair (ordered from smallest to largest) of the diagonal elements of the matrix. [3] But one eigenvalue, falling after the last diagonal element, sometimes leaves the domain of the diagonal elements.

This last eigenvalue poses a unique problem. The strengths associated with all eigenvalues within the domain of diagonal elements can be shown to be independent of the order of the subset matrices. The strength associated with an eigenvalue is found by squaring the components of the corresponding eigenvector, adding them together and taking the square root. The strength associated with this last eigenvalue, however, is proportional to the order of the subset matrix. Thus, the strength associated with the eigenvalue falling outside the domain of diagonal elements must be treated separately. It is important to note that only eigenvectors have strengths and that each eigenvector also has a unique eigenvalue associated with it.

The program that diagonalizes the matrices was written at Argonne National Laboratory [4]. The programs that randomly pick diagonal elements, set up the subset matrix, find the strengths of the eigenvectors and store the eigenvalues and strengths for averaging later, coded in FORTRAN, were written as part of this project.

An iteration consists of a run through the programs. Each iteration yields eigenvectors, eigenvalues and strengths calculated from each eigenvector for one subset matrix. The eigenvectors, eigenvalues and strengths of the eigenvectors for each iteration are stored and later averaged together so that better results are obtained.

RESULTS

The program that diagonalized the subset matrices produces eigenvalues and eigenvectors from the subset matrices. These eigenvalues and eigenvectors are then summed into histograms. All of the runs (or iterations) are averaged together within the histograms to minimize errors introduced by the random nature of the Monte Carlo method.

Graphs were plotted for many runs through the programs. The graphs of the eigenvalues against the strengths of the eigenvectors associated with the eigenvalues were the main interest of this research. This relationship was important because it shows which eigenvalues are in the domain of diagonal elements. Often all but the last eigenvalue was in the domain of diagonal elements.

Several trends were noticed in working with the parameters affecting the results:

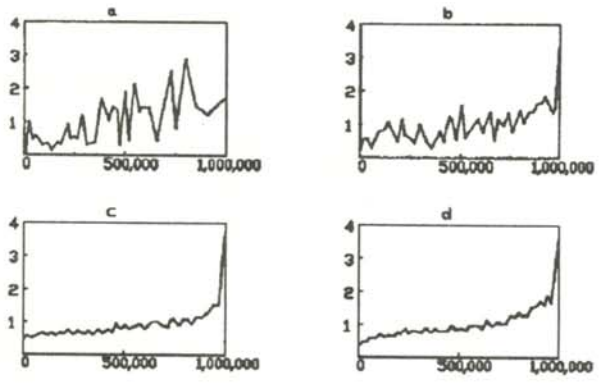

Figure 1

Graphs of strength of eigenvector versus respective eigenvalue. The matrix (of order 10^6) has: diagonal terms evenly spaced between 1 and 10^6 and off diagonal terms = 0.1. The sub-matrix size is 100. The four graphs show the general trend as the number of iterations is increased. 1a) Only 1 iteration. 1b) 10 iterations averaged together, 1c) 100 iterations averaged together. 1d) 200 iterations averaged together. Note that there is a general convergence towards a smooth curve as the number of iterations averaged together increases. This deviation from a smooth curve followed the standard Monte-Carlo proportionality: deviation = constant / (Number of iterations)$^{1/2}$.

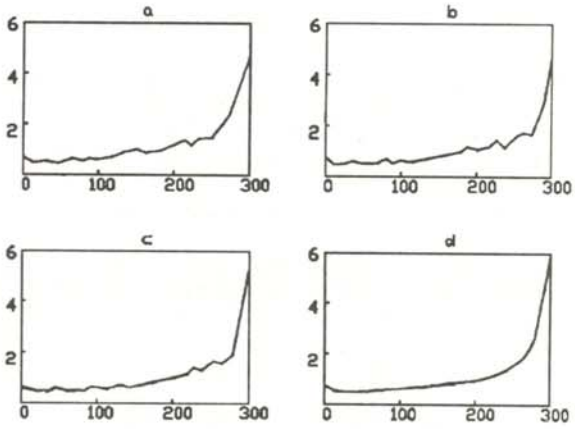

Figure 2

Graphs of strengths of the eigenvector as a function of the eigenvalue. The matrix (of order 290) has diagonal elements evenly spaced between 1 and 290 and off diagonal elements equal to 0.1. 2a) Sub-matrix of order 25. 2b) Sub-matrix of order 50. 2c) Sub-matrix of order 100. 2d) Main matrix of order 290, the exact answer. These graphs show the effects of the subset matrix size on the results. The number of iterations was set so that the same amount of points (1000) was used in all cases. The difference between graphs 2a) and 2d) are significant, i.e. greater than the random Monte-Carlo deviations, but the general pattern is quite clear. This general pattern is clear for a sub-matrix order of greater than about 10.

1) As the number of iterations increases, the smoothness of the graph increases (see Figure 1). This is a general result of all Monte-Carlo methods: as the number of iterations increases, the random fluctuations average out to a smooth curve.
2) As the subset matrices' size (M) approaches the matrix size (N), the graph of the subset matrix looks more like the original matrix graph. This should be obvious: as the subsets become more like the main matrix, the subsets' results will become more like the main matrix's results.

Figure 1 shows how increasing the number of iterations decreases deviations. Precision is improved because more samples of the main matrix, or order 10^6, are used. The main matrix could not be diagonalized because it was too large for our computer. By the time 100 iterations are averaged together, much of the deviation shown for one iteration is lost. The sub-matrix size was 100 for the 4 parts of Figure 1.

Figure 2 shows the effect of the subset matrix size. A matrix of size 290 is diagonalized without using the Monte-Carlo method and compared to several that were. The general trends of the actual graph may be seen even when the subset matrix is of size 25. Thus, in this test problem, the general goal of obtaining the trends is met even when the subset matrix size is only 25. The resemblance improves for subset matrix sizes of 50 and 100. The same number of subset matrices, 1000, was used each time, so that the effect of the subset matrix size could be determined.

Two numbers, the sub-matrices' size (M) and the number of iterations averaged together (ITER), determine the time needed to get an answer and the amount of random fluctuations. The execution time is proportional to the cube of the order of the subset matrix (M^3). The size of the random fluctuations is proportional to $1/(M*ITER)^{.5}$. Thus, there is a trade-off between an acceptable amount of fluctuation and an acceptable running time.

As the size of the variations among the off-diagonal elements increases, more than one eigenvalue can fall out of the domain of diagonal elements. A clear algorithm has yet to be developed to analyze these extra eigenvalues and their associated eigenvectors' strength.

ACKNOWLEDGMENTS

Many of the computer runs were performed by Jennifer Kennelly (Heelan High School, Sioux City, IA). Her help enabled the completion of many more tests. Professor Groh led the way and did much of the programming.

REFERENCES

† Support for this project was provided by the Iowa Public Service Company Science Education and Undergraduate Research Program grant to Morningside College.

1. D.J. Groh, et. al., 'An Approximation Method for Eigenvectors of Very Large Matrices', to be published in J. of Scientific Comp.

2. P.C. Shields, Elementary Linear Algebra, Worth Publishers, New York, 1980. or G. Arfken, Mathematical Methods for Physicists, Academic Press, New York, 1970.

3. C. Kittel, Quantum Theory of Solids, John Wiley and Sons, New York, 1963.

4. P. S. Garbow, Applied Mathematics Division, Argonne National Laboratory, Argonne, Il 60439.

FACULTY SPONSOR

Dr. David Groh
Physics Department
Morningside College
Sioux City, IA 51106

PARAMETERIZING A DIMINISHED FORMATION ZONE DUE TO MULTIPLE SCATTERING IN THE THEORY OF TRANSITION RADIATION

A.L. McKnight
Physics Department
Roanoke College
Salem, VA 24153
Received April 28, 1991

ABSTRACT

In a recent study [1] of how radiation fields associated with transition radiation from a plasma-like non-stationary medium are distorted due to multiple scattering (which act to withdraw the traversing particle from the formation zone), a dimensionless parameter ($\eta \leq 1$) is introduced to describe the degree of 'withdrawness'. The parameter η is defined as $1/(1 + f)$ where f is a function of the input parameters (the Lorentz factor γ and the scattering angle θ_s) and the observables (angle θ and the frequency ω of the emitted photon) and the plasma frequency of the medium ω_p. In this article, we analyze the extreme and asymptotic behavior of η and its 2-dimensional normalization subject to energy constraints.

1. A.F. Barghouty and M.J. Pantazopoulou, Phys.Rev., A44, 1991, p. 3083.

INTRODUCTION

Experiments measuring radiation associated with the passage of charged particles through media under homogeneous or inhomogeneous conditions measure a sum of many classical radiative processes, including Cerenkov radiation, bremsstrahlung and transition radiation. Cerenkov radiation is the optical emission of a charge moving with a constant velocity larger than the phase velocity of light in a medium. Transition radiation, due to the movement of a relativistic charged particle with constant velocity under inhomogeneous conditions [1,2], is more akin to bremsstrahlung than Cerenkov radiation. It requires only a change in the parameter vn/c, where n is the index of refraction and v is the velocity of the traversing particle. The simplest process satisfying this condition is when a charge crosses the boundary between a vacuum and a medium[2]. Transition radiation is an emission process associated with inhomogeneities (both temporal and spatial) in the medium.

Earlier treatments of transition radiation concentrate on the case of a static interface between two media, either medium-medium or vacuum-medium [1,2]. In the case of vacuum-medium transitions, a differential radiation intensity is derived in the relativistic limit [2]:

$$\frac{d^2 I}{d\theta\, d\omega} = \frac{\alpha\, h}{\pi^2}\, \theta^3\, (\omega c)^2\, (l_v - l_m)^2 \quad , \tag{1}$$

where θ is the angle formed between the emitted photon and the traversing particle. l_m and l_v are the coherent lengths in medium and vacuum, given by:

$$l_v \approx \frac{4\,c}{\omega}\, (\gamma^{-2} + \theta^2)^{-1}$$

$$l_m \approx \frac{4\,c}{\omega} \left(\gamma^{-2} + \theta^2 + \frac{\omega_p^2}{\omega^2} \right)^{-1} \quad , \tag{2}$$

where γ is the Lorentz factor for the traversing particle and ω_p is the plasma frequency of the medium. Essentially l_m and l_v determine the size of the formation zone of the radiation field, i.e., the distance along the particle trajectory after which separation between the particle and the emitted photon is of the order of the photon wavelength.

A recent study [3] examined a dynamic-interface model,

Andrew is a senior, double majoring in chemistry and spanish. He is a member of the Roanoke College Honors Program. This project came out of research he did in the summer and fall of 1990 at Roanoke. Andrew also took part in an inorganic synthesis project last summer at Rice University. After graduating in May with a B.Sc., Andrew looks forward to beginning work on his Ph.D. in inorganic chemistry.

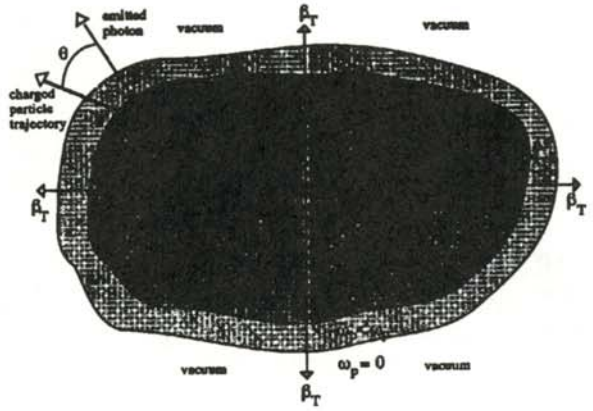

Figure 1
Schematic showing the isotropically expanding medium (with thermal expansion velocity β_T) and its transition to vacuum. The transition zone appears due to the jump in ε. The traversing charged particle 'sees' this dynamic interface and emits a photon even before it actually crosses the boundary.

where a plasma-like medium is allowed to expand freely and isotropically. The medium makes a 'jump, characterized by an abrupt change in the dielectric permittivity ε, and thus the value of nv/c makes a sudden change. This 'jump' is seen as a 'transition zone', with a time scale and size (Δt, Δz).

To explain this further, we envision an isotropically expanding medium with thermal expansion velocity β_T (see Figure 1). As the medium expands, its density decreases. This decrease in density will lower the plasma frequency of the medium. A traversing charged particle, with velocity » β_T, thus will experience a medium making an abrupt change in its ε. Because this happens over finite time Δt (and corresponding finite distance Δz), we treat this as a distinct evolutionary stage of the medium, different from the original medium and the vacuum, and call it the 'transition zone'. Over this transition zone, we calculate an average density that gives rise to an average plasma frequency $<\omega_p>$.

This dynamic-interface model contains 3 media (medium, transition zone, and vacuum) and 2 boundaries. The length in the transition zone is given by [3]:

$$l_T \approx \frac{4c}{\omega}\left(\gamma^{-2} + \theta^2 + \frac{<\omega_p>^2}{\omega^2}\right)^{-1}, \qquad (3)$$

where $<\omega_p>$ is plasma frequency of the medium averaged over the transition zone.

Multiple scattering, defined as multiple long-range, small angle elastic Coulomb collisions between the particles of the medium and the traversing particle, results in a diminishing of the coherent length in the medium. This tends to withdraw the particle from the formation zone. This diminishing is parameterized by [3]

$$l'_m = \eta\, l_m , \qquad (4)$$

where l'_m is the new coherent length in the medium and η is a dimensionless parameter defined by [3]:

$$\eta = \frac{1}{1 + <\theta_s^2>\left(\gamma^{-2} + \theta^2 + \frac{<\omega_p>^2}{\omega^2}\right)^{-1}}, \qquad (5)$$

where $<\theta_s^2>$ is the mean square of the scattering angle over the length l_m. The parameter η varies from a non-zero asymptotic value to one. The differential radiation intensity was derived in the relativistic limit for the dynamic-interface model [3]:

$$\frac{d^2 I}{d\theta\, d\omega} = \frac{\alpha h}{\pi^2}\theta^3 (\omega c)^2 (l'_v - l_m)^2 \left| 1 + \frac{l_T - l_v}{l_m - l_T} e^{-2i\frac{\Delta z}{l_T}} \right|^2 . \qquad (6)$$

Numerical solutions to Equation 6 show that multiple scattering represents a marked and advantageous effect in differentiating among the competing radiation mechanisms.

ANALYSIS OF η

We begin by studying the dependence of η on θ (the angle between the emitted photon and the traversing particle) and ω (the frequency of the emitted photon). We do this twice, once by a contour plot of η(θ,ω) and also by

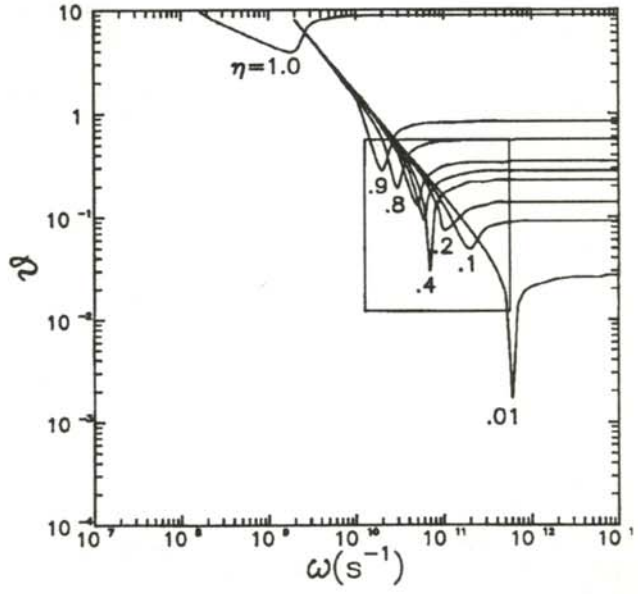

Figure 2
Contour plot of η (parameterizing the degree of withdrawness from the formation zone) as a function of θ and ω, calculated using Equation 5.

averaging over angle and frequency, one variable at a time:

$$\langle\eta\rangle_\theta = \int_0^{2\pi} \frac{\eta(\theta,\omega)}{2\pi}\, d\theta$$

$$\langle\eta\rangle_\omega = \int_0^{\gamma\omega_p} \frac{\eta(\theta,\omega)}{\gamma\,\omega_p}\, d\omega\ . \qquad (7)$$

The upper limit for integrating over ω is taken to be the cutoff frequency $\gamma\omega_p$ because the radiation intensity drops rapidly beyond this frequency. After this, we derive expressions for ω and θ that minimize η using the Lagrange undetermined multiplier method. Finally, to conserve energy in the process, we derive a 2-dimensional (θ and ω) normalization factor for η.

Figure 2 is contour plot of η as a function of ω and θ (Equation 5) that uses an estimate [3] for $\langle\theta_s^2\rangle$. The frequency and angular ranges inside the box in Figure 2 show where η deviates from 1, signifying an appreciable effect of multiple scattering over the over the frequency range of $(1/(\gamma^{-1}\Delta t),\gamma\langle\omega_p\rangle)$ and the angular range $(\gamma^{-1}, \langle\theta_s^2\rangle^{.5})$

Figure 3 shows the $\langle\eta\rangle_\theta$ versus the frequency of the emitted photon. The integration was done numerically using Gaussian quadrature[4]. η begins to deviate from unity (parameterizing a non-diminished formation zone) for frequencies above a threshold frequency $1/(\gamma^{-1}\Delta t)$.

Figure 4 shows a smooth, parametric function of frequency over the wide range $(1/(\gamma^{-1}\Delta t),\gamma\langle\omega_p\rangle)$. It appears to saturate and persist for frequencies above $\gamma\langle\omega_p\rangle$.

Figure 4 shows $\langle\eta\rangle_\omega$ as a function of the photon angle.

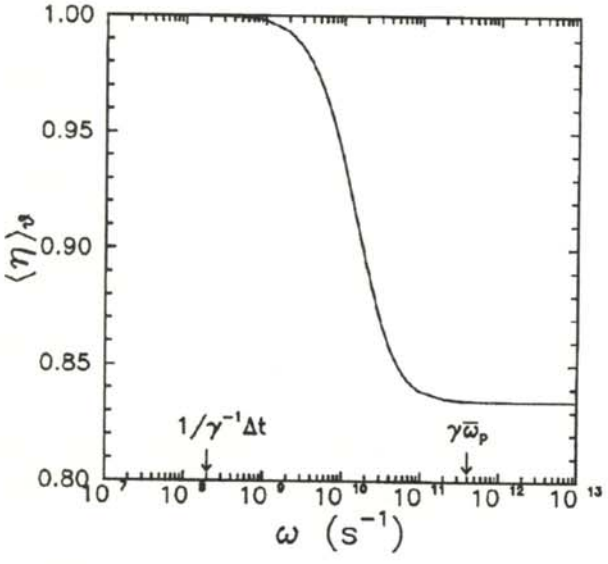

Figure 3
Angle integrated $\langle\eta\rangle_\theta$ as a function of the frequency of the emitted photon.

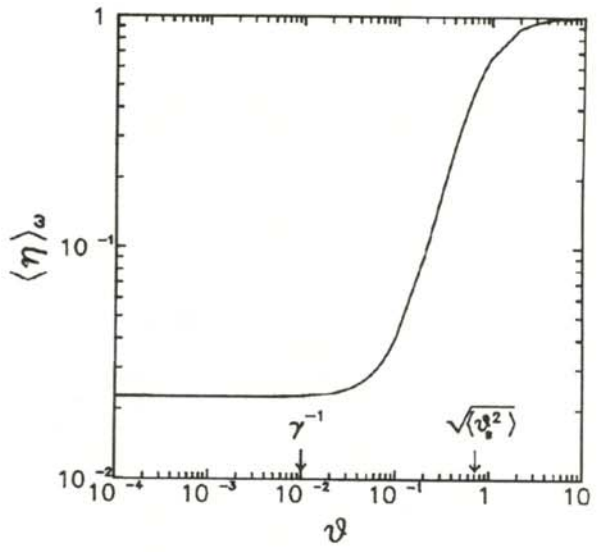

Figure 4
Frequency integrated $\langle\eta\rangle_\omega$ as a function of the angle of the emitted photon.

For angles $\leq \gamma^{-1}$, η is far from unity, indicating a strong diminishing effect on the formation zone. Over the angular range $(\gamma^{-1}, \langle\theta_s^2\rangle^{.5})$, the same smooth, parametric behavior is seen as in Figure 3. These figures suggest a diminished formation zone due to multiple scattering over the frequency range $(1/(\gamma^{-1}\Delta t),\gamma\langle\omega_p\rangle)$ and the angular range $(\gamma^{-1}, \langle\theta_s^2\rangle^{.5})$. Assuming that the collisions (i.e. uncorrelated, near collisions neglecting bremsstrahlung[3]) do not depend on the frequency nor the angle of the emitted photon, the constraint due to conservation of energy can be written as:

$$\frac{d^2 I'}{d\theta\, d\omega} - \frac{d^2 I}{d\theta\, d\omega} = 0\ , \qquad (8)$$

where the I ' refers to the inclusion of multiple scattering. Using the results of Equations 1 and 6 gives:

$$\frac{\alpha\, h}{\pi^2}\,\theta^3\,(\omega\, c)^2\,[l_m(\eta - 1)]$$

$$[l_m(\eta+1) - 2\, l_T + 2(l_T - l_v)\cos\phi] = 0\ , \qquad (9)$$

where $\phi = 2\Delta z/l_T$ is the imaginary part of the phase factor appearing in Equations 1 and 6. This yields the constraint:

$$\cos\phi = \frac{l_T - \zeta\, l_m}{l_T - l_v}\ , \qquad (10)$$

where $\zeta = (\eta+1)/2$

With this constraint, the Lagrange method gives the expression

$$F(\zeta,\phi,\lambda) = \frac{(2\zeta - 1) - \lambda(\cos\phi - l_T - \zeta l_m)}{(l_T - l_m)} \quad (11)$$

where λ is the Lagrange multiplier. Setting the partial derivatives of Equation 11 equal to zero and solving for λ gives:

$$\omega\left(\gamma^{-2} + \theta^2 + \frac{<\omega_p>^2}{\omega^2}\right) = \frac{2\pi m c}{\Delta z}, \quad m = 1, 2, \ldots \quad (12)$$

By substituting values for the input parameters (of reference 3) and averaging over each variable separately, we find in Figure 3 that ω increases for increasing m, beginning with $\omega = \gamma\omega_p$, corresponding to m = 1. Additionally, in Figure 4, we find that as m increases, θ decreases with $\theta = \gamma^{-1}$ corresponding to m = 1. In both cases, and as m becomes exceedingly large, the increase (decrease) in ω (θ) is monotonic as the difference between two successive values becomes exceedingly small. This behavior depicted by Figures 3 and 4, shows that the effect of multiple scattering, when maximized, tends to saturate at these values of ω and θ that minimize η, giving it its asymptotic value.

For the purpose of energy conservation, a 2-dimensional (ω and θ) normalization of η is done using a two-dimensional Simpson's integration routine[4]. Integrating Equation 5 over both θ and ω, and once again assuming values for the input parameters[3] gives a value of 0.8346. An examination of Figures 2 and 3 seems to indicate that η is more sensitive to θ than it is to ω, since Figure 3 is an average over θ , thus 'removing' that dependence leaving η minimized at a value almost equal to 0.83, while Figure 2 shows η is still far from saturation after averaging over ω. This feature of η seems to suggest that the effect of multiple scattering is largely geometric rather than dispersive, making it of significance for those emission processes directly affected by the formation-zone, e.g. in the calculation of X-ray emissivity of relativistic electrons traversing cosmic grains. Here, the formation-zone effect has been found [5,6] to suppress high frequency transition radiation.

ACKNOWLEDGEMENTS

The author would like to thank Dr. A.F. Barghouty of Roanoke College for his helpful insight and support through out the process of this work and for his patient review of the manuscript

REFERENCES

1. V.L. Ginzburg and V.N. Tsyovich, Phys. Rep. 49, 1979, p. 1.

2. M.L. Ter-Mikaelian, High-Energy Electrodynamic Processes in Condensed Media, Wiley-Interscience, New York, 1972, Chapter 4.

3. A.F. Barghouty and M.J. Pantazopoulou, Phys.Rev. A44, , 1991, p. 3083.

4. W.H. Press, B.P. Flannery, S.A. Teukolsky and W.T. Vetterling, Numerical Recipes, Cambridge University Press, New York, 1986.

5. G.B. Yodh, X. Artru and R. Ramaty, Astrophys. J. 181, 1973, p. 725.

6. L. Durand, Astrophys. J. 182, 1973, p. 417.

FACULTY SPONSOR

Dr. A.F. Barghouty
Department of Physics
Roanoke College
Salem, VA 24153

SHORT-TERM PREDICTION OF SMOOTHED SUNSPOT NUMBERS USING CHAOTIC ANALYSIS †

Eiluned A. Hogenson
Physics Department
University of Alaska Fairbanks
Fairbanks, AK 99775-1320

Submitted September 15, 1991

ABSTRACT

This paper will give an overview of the concepts behind strange attractors, fractal dimension, correlation dimension and Lyapunov exponents, and how they apply, in particular, to the dynamical system described by the sequence of smoothed sunspot numbers. Various methods of chaotic prediction will be discussed. The smoothed monthly sunspot numbers will be predicted from the current number to December 1997.

Sunspots are solar photospheric phenomena which are darker than the surrounding photosphere because they are about 1500K cooler, due to a strong magnetic field which inhibits the convective transport of energy. They have been recorded for millenia. There are Chinese oracle bones dating from before 1000 B.C. which record sunspots[1]. For many centuries sunspots were believed to be the transit of planets, possibly because of Aristotle's belief that the sun was a perfect body, and so could have no blemishes[2]. With the invention of the telescope in the early 17th century, sunspots were finally recognized as solar features[3]. However, it was much later, in 1843, that the sunspots were recognized as having a cycle of approximately 11 years[4]. The true cycle is 11.13 years. [5].

In 1848, the sunspot-relative numbers as a measure of these sunspots were introduced. The numbers are calculated by counting the number of individual spots, f, and counting the number of groups of spots, g. The sunspot number is given by $k(10g + f)$, where k was originally set to unity, but because today we are able to see more sunspots due to more sighting stations and better equipment, the value of this constant is set to $k=0.6$[6].

Sunspots are a relative measure of solar activity. Because of this, it is useful to monitor and predict them[7-14]. For instance, an incorrect prediction of the solar cycle may have contributed to the premature death of the Skylab satellite, as the density of air at the height Skylab was operating varies with the solar cycle[15].

Another reason to study sunspots is that they may be correlated with weather on Earth. The famous example of this is the "Maunder minimum", a period stretching from about 1645 to 1715 where there were few sunspots sighted[16,17]. This corresponds to the coldest period of the "Little Ice Age" which was characterized by an extreme temperature dip[17]. The annual sunspot numbers, with the Maunder minimum of the 17th century, are shown in Figure 1. The data before 1650 is pieced together from phenomena related to the solar cycle, such as observed auroras, in addition to direct sunspot sightings[2].

The sun rotates with a period of about 27 days, so the daily sunspot data have fluctuations which depend on which side of the sun is facing Earth. These daily fluctuations are mostly independent of the variation in the solar

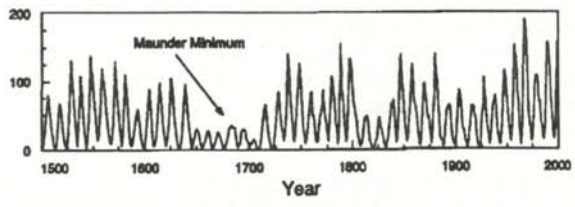

Figure 1
Mean yearly sunspot numbers from 1500 to 1900 AD. Data before 1650 have been pieced together from phenomena relating to the solar cycle as well as direct sunspot sightings.

Eiluned is a senior majoring in physics. She and her husband are planning to join the Peace Corps after their graduation. This project was the result of a summer internship at the Geophysical Institute in Fairbanks, Alaska.

cycle. The most useful prediction, then, is that of the monthly sunspot number. Usually what is predicted is the smoothed monthly sunspot number[7,10,13] which is the result of the observed monthly numbers for 13 months $\{R_{-6}, \ldots R_0, \ldots, R_{+6}\}$ smoothed with the following formula:

$$S_0 \frac{R_{-6} + R_{+6} + 2\sum_{I=-5}^{+5} R_i}{24} . \qquad (1)$$

There were no reliable monthly sunspot numbers recorded before 1749, however, so there are only 2907 raw sunspot numbers available (January 1749 through March 1991), which correspond to 2895 smoothed data.

Others have used chaotic analysis to predict sunspot cycles, [13,14] but because of the choices of data sets, the results had limited applicability. The smoothed sunspot number is used in this paper as it is the one which is usually used for prediction. Also, the averaging reduces some of the noise inherent in the raw data. This is a small data set for doing chaotic analysis[18,19] but some consider even data sets containing as few as 500 points to be adequate[20].

AN INTRODUCTION TO CHAOS

What differentiates chaotic systems from other dynamical systems is the sustained sensitivity to initial conditions. In chaotic systems, if a state is initially similar to another state, there is no guarantee that the final states will be similar. This sensitivity to initial conditions arises because there are nonlinear terms in the underlying dynamics of the system. Sensitivity to initial conditions does not imply that chaotic systems have as their source random processes. The only fundamental source of randomness occurs in quantum mechanics. In principle, every macroscopic system is deterministic, including chaotic systems[21]. Lorenz's research into a system of equations which modelled circulation of fluids was the first physical investigation into deterministic chaotic phenomenon[22]. In his paper was also the first drawing of a chaotic attractor.

The attractor is the region in phase space which confines the system, once a sufficient time has passed. If the system is chaotic, the attractor is often called "strange", and usually has a complex geometrical structure. The attractors of a chaotic systems must be nonperiodic. They represent an infinite line confined to a finite area. Thus, the dimension of a strange attractor cannot be measured in the ordinary way. Strange attractors must have fractal dimension, a concept introduced by Mandelbrot[23]. When the fractal dimension is an integer it corresponds to the common definition of dimension.

Finding the approximate fractal dimension will be useful in studying the sunspot attractor, because a non-integer fractal dimension is symptomatic of a chaotic system. Unfortunately, finding a non-integer fractal dimension is not always conclusive, as the error bounds on the dimension calculated may include an integer value.

There is another, more reliable test for chaos: the presence of a positive Lyapunov exponent. Lyapunov exponents are indicators of a system's sensitivity to initial conditions. They measure how quickly nearby points on the attractor diverge from or converge to each other. If the system is sensitive to initial values, the divergence of nearby points will be rapid, and at least one Lyapunov exponent will be positive. Otherwise, the Lyapunov exponents will be not positive[24,25]. A more complete introduction to chaos can be found elsewhere[26-29].

RECONSTRUCTING THE ATTRACTOR

It is not always possible to measure all of the variables in the system. Usually only one variable is measured in the form of a time-series. Fortunately, using vectors made from time delayed values of a single time series, the attractor may be reconstructed.[30,31] This reconstructed attractor has the same geometric properties as the original attractor. Note, however, that the axes in reconstructed space have no physical meaning *per se*. For instance the time series $\{x_1, x_2, \ldots, x_j, \ldots, x_N\}$, would yield reconstructed vectors:

$$\mathbf{X}_j = (x_j, x_{j+\tau}, x_{j+2\tau}, \ldots x_{j+(D-1)\tau}) , \qquad (2)$$

where D is the embedding dimension. The points $\{\mathbf{X}_j\}$ are D-dimensional points on the reconstructed attractor. As the index j is increased, the trajectory traced in the reconstructed phase space defines the reconstructed attractor. Choosing the delay time τ is tricky, and greatly influences the attractor's shape if noise is present in the data or if there are a limited number of points. Both of these problems are present in the smoothed sunspot data set. If τ is too short the coordinates become singular, $x_j \approx x_{j+\tau}$, and the points $\{\mathbf{X}_j\}$ lie stretched along the diagonal in phase space. As an example of this, Figure 2a shows a 3 dimensional reconstruction of the smoothed sunspot attractor, using a delay of τ = 3 months. On the other hand, if the delay is too long, chaos causes x_j and $x_{j+(D-1)\tau}$ to be causally disconnected, and the attractor shows no obvious form[21]. Figure 2b shows the 3 dimensional reconstruction with a delay which is too large, τ = 50 months. Compare Figures 2a and 2b with Figure 2c which is a reconstruction of the smoothed sunspot attractor using τ = 7 months. This choice of τ yields an attractor which has a greater separation between the trajectory segments than

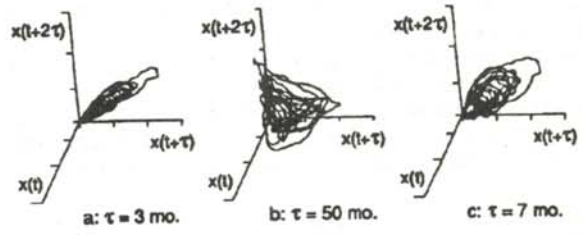

Figure 2

Reconstructions of the smoothed sunspot attractor for various delay times, embedding dimension of 3. a) attractor is stretched along the diagonal for a delay time of 3 months. b) attractor is disorganized for a delay time of 50 months. c) delay time of 7 months has greater trajectory segment separation than in a) and is more organized than the attractor in b).

that shown in Figure 2a, yet it has more organization than the attractor shown in Figure 2b. In the next section, we will discuss how suitable τ and D are chosen.

QUANTIFYING THE DIMENSION OF THE ATTRACTOR

The sunspot attractor is roughly confined to a plane, but has points which protrude from that plane. Consequently, it should have a fractal dimension between 2 and 3.

To find this dimension, one first must calculate the correlation integral:

$$C(r) = \lim_{N\to\infty} \frac{1}{N^2} \sum_{i=1}^{N} \Theta\,(r - |\,\mathbf{X}_i - \mathbf{X}_j\,|)\,, \qquad (3)$$

where the $|\mathbf{X}_i - \mathbf{X}_j|$ denote the Euclidean distance between the two vectors and Θ is the Heaviside function, defined by:

$$\Theta(x) = \begin{cases} 0 & x<0 \\ 1 & x\geq 0 \end{cases}. \qquad (4)$$

The correlation integral behaves as $C(r) \alpha r^d$ for small r. This result defines d, the correlation dimension. The correlation dimension has been shown to be a close lower bound to the fractal dimension[32], and consequently it is often calculated in place of the fractal dimension. Since N does not go to infinity, we find the correlation dimension from the slope of log(r) vs. log(C(r)),

$$d = \frac{\Delta \log[C(r)]}{\Delta \log(r)}\,. \qquad (5)$$

The slope will not be constant along the entire range of r, since the data set is finite. There is some maximum distance, r_{max}, which encloses the entire attractor. Consequently, radii larger than r_{max} produce the same value for C(r), i.e., the slope goes to zero for $r>r_{max}$. The lower range of the plot is affected by the presence of noise, as the smaller distances between points are more influenced proportionately by noise than the larger ones. Above the noise region and below the region of zero slope, there will be a range where the slope is fairly constant. This is called the "scaling region", and is where the correlated dimension is measured.

For small data sets, a slightly altered algorithm for calculating the correlation integral yields a larger scaling regions[20]. This method involves finding $r_j(m)$ or the radius of a sphere about $\mathbf{X}_j$ which contains m points on the attractor. The radius $r_j(m)$ is dependent on which reference point $\mathbf{X}_j$ we choose. To obtain the correlation dimension from this set, we use

$$D = \frac{\Delta \log (m)}{\Delta \log[\langle r(m)\rangle]}\,, \qquad (6)$$

where the sharp brackets refer to averaging the set $\{r_j(m)\}$ along lines of constant m (horizontal averaging). This is equivalent to finding the average radius of a sphere, centered on a point on the attractor, which encloses m neighboring points. The correlation dimension estimate becomes larger as we embed the data in higher and higher dimensions, until saturation is reached and the slopes converge to d. Thus, we must calculate the correlation dimension for different embedding dimensions. In Figure 3, we show the derivatives of the correlation integrals for

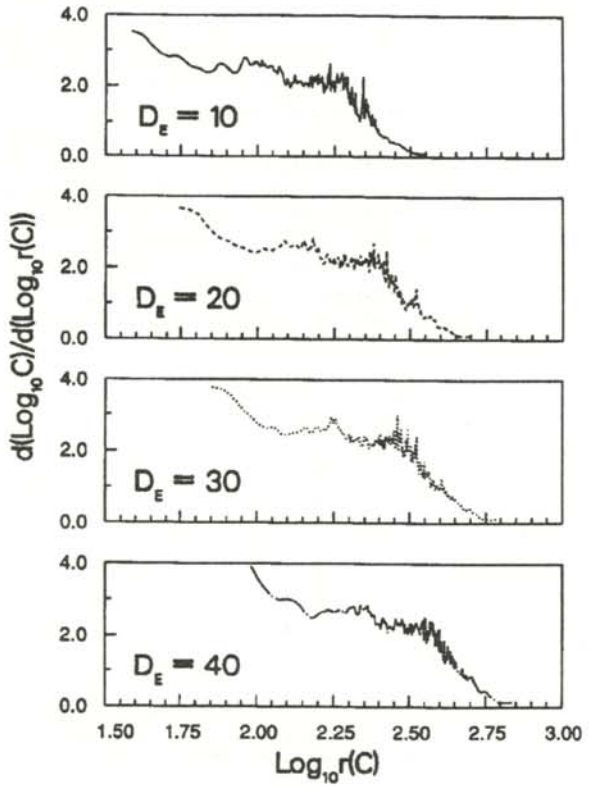

Figure 3
The derivatives of the correlation integrals for various embeddings: 10, 20, 30, 40. The scaling region can be seen where the derivative becomes flat.

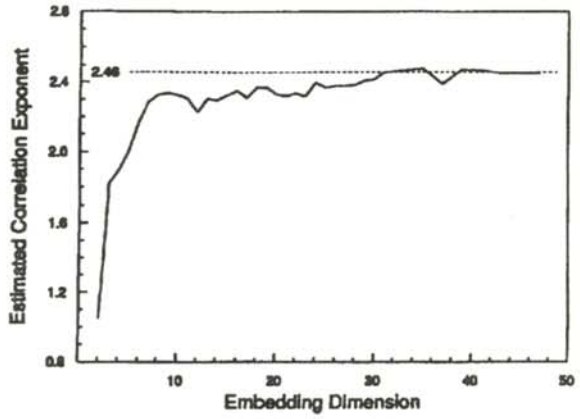

Figure 4
Correlation estimate as a function of embedding dimension. Estimate saturates around embedding dimension 30. Averaging the estimates for embedding dimensions larger than 30 yields a value of 2.46.

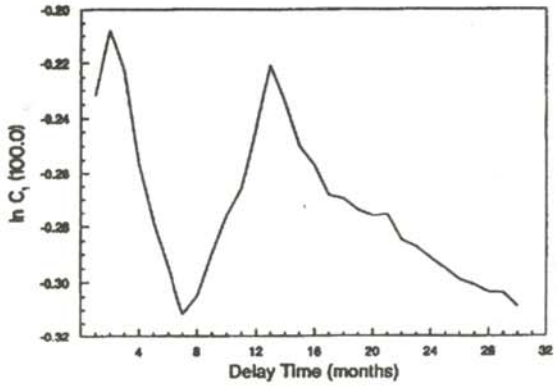

Figure 5
The minium of the generalized correlation integral with q=1 occurs for a delay time of 7 months.

various embedding dimensions.

For the smoothed sunspot data, saturation was reached only after moving to an embedding dimension of about 30, yielding a value for the correlation dimension of $d \approx 2.5$ (see Figure 4). Because the correlation dimension is a close lower bound to the fractal dimension, we can say with a fair amount of certainty that the sunspot attractor need only be embedded in 3 dimension for a complete reconstruction.

The next parameter that must be calculated is the time delay τ. This is done by introducing a parameter known as the "mutual information". [33] It measures the general dependence of two variables. By picking a minimum of this function, we choose a delay that does not create vectors that are too related in the reconstructed attractor and keeps the attractor organized. The first minimum is selected because a short time delay usually yields a longer scaling region.

The first minimum of the mutual information, can be found using the generalized correlation integral[34]:

$$C_q(r) = \left(\frac{1}{N} \sum_{j=1}^{N} P_r^{(q-1)}(X_j) \right)^{\frac{1}{(q-1)}} , \qquad (7)$$

where $P_r(X_j)$ is the probability to find other points within a sphere of radius r centered about X_j:

$$P_r(X_j) = \frac{1}{N} \sum_{k=1}^{N} \Theta(r - | X_j - X_k |) . \qquad (8)$$

This counts the points which lie within r of the reference vector X_j and divides by the number of points in the data set. The minima of the mutual information are also the minima of the logarithm of this generalized correlation with q=1. Figure 5 shows that the first minimum occurs for a delay time of 7 months, using D=10 and r=100.0. Notice that the correlation integral, Equation 3 is just this generalized correlation integral with q=2.

QUANTIFYING THE CHAOS

The Lyapunov exponents quantify the amount by which neighboring trajectories diverge on the attractor per time step. If a D-dimensional infinitesimal sphere is chosen at t=0, we may record the Lyapunov exponents by how the sphere deforms into an D-dimensional ellipsoid with principal axes $\{p_j\}$ as time progresses, due to the divergence and convergence of the flow. The Lyapunov exponents $\{\lambda_j\}$ are defined by :

$$\lambda_1 = \lim_{t \to \infty} \frac{1}{t} \log_2 \frac{p_i(t)}{p_i(0)} . \qquad (9)$$

The exponents are ranked in order from largest to smallest. A positive exponent marks a divergence of nearby trajectories, and a negative exponent marks a convergence. Thus, the Lyapunov exponents are a good indicator of chaos. Any system which has a positive λ_1 is defined to be chaotic[24]. Since the system is embedded in D dimensions, there are D directions in which the system can diverge or converge. Consequently there are D Lyapunov exponents associated with the system.

Long term behavior of the system is primarily determined to be the largest positive Lyapunov exponent. The value calculated[24] for λ_1 depends on the initial position on the attractor. By incrementing the starting position, we computed a distribution of values for λ_1. The results of the calculations for different starting values are shown in Figure 6. The value for λ_1 was found to be .009 ±.002 bits/month. The positive value provides verification that the attractor is chaotic.

PREDICTION

Predicting chaotic systems may seem impossible due to the divergence of nearby trajectory segments. However, chaos is deterministic, and since the Lyapunov exponent is fairly small we can make short range predictions which, as we will show, are often fairly accurate. With a noise-free system, the inverse of the Lyapunov exponent

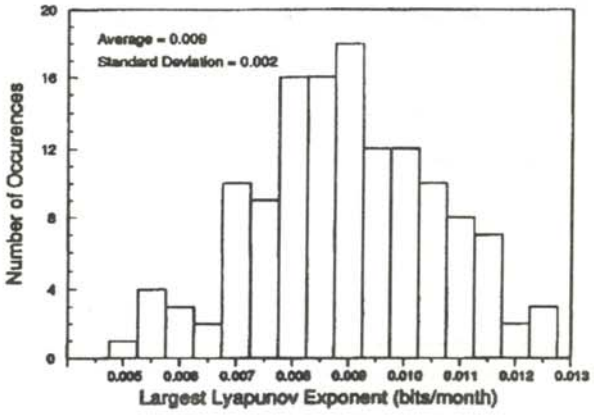

Figure 6
Histogram showing distribution of values for the largest Lyapunov exponent in units of bits/month using a delay time of 7 months and an embedding dimension of 3.

is the upper limit to the range of reliable predictions. We can use this to put an absolute upper bound on our ability to predict the sunspot cycle, $T_{max} \leq \ln(2)/\lambda_1 \approx 20$ years.

One simple approach to predicting the future state of the system is to assume that the system will follow the path of its nearest neighbor on the attractor. This is termed a zeroth-order prediction.[35] First-order prediction is also based on the principle that a point on the attractor will do what its nearest neighbors do, but it uses a number of surrounding neighbors greater than D. There are two slightly different versions of local-linear prediction. In direct prediction the coordinates of the neighbors are placed in a matrix, $\mathbf{C_o}$, and the evolution of the neighbors T time steps into the future is recorded in the vector $\mathbf{D_T}$, which contains the final coordinates. Then we find the vector $\mathbf{m}$ which best maps the present state into the future,

$$\mathbf{C_o} \cdot \mathbf{m} = \mathbf{D_T}, \tag{10}$$

Once we have the vector $\mathbf{m}$, we can predict the future of the point, x_{pred}, by:[35]

$$x_{pred} = \mathbf{x_o} \cdot \mathbf{m}. \tag{11}$$

In iterative forecasting, the time step is one, and the process for direct forecasting is repeated T times. This would cause the prediction to evolve like the system and is usually more accurate than direct forecasting when there is no noise present. In the presence of noise, however, this method suffers.

These three methods of prediction were used on the smoothed sunspot data. To gauge the error involved, we calculated the normalized error E, which is the difference between the predicted value and the actual value normalized by the rms deviation of the data:

$$E = \sqrt{\frac{\langle (x_{pred} - x_T)^2 \rangle}{\langle (x - \langle x \rangle)^2 \rangle}}. \tag{12}$$

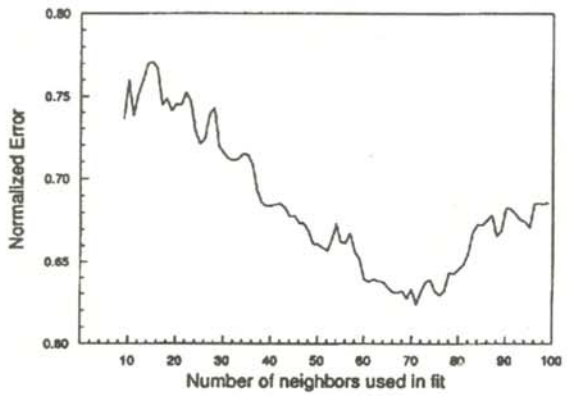

Figure 7
Number of neighbors used in the local-linear direct prediction method versus the normalized error, using a time step of 24 months. The graph show a minimum at around 70 neighbors.

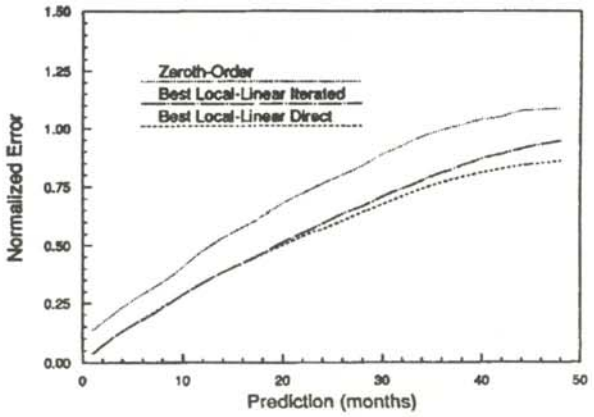

Figure 8
A comparison of the chaotic prediction methods discussed: Zeroth-order, first-order iterated and first-order direct.

If E = 0, there is no difference between the actual value and the predicted value. If E = 1, the prediction is no better than the average value of the data.

When predicting with the smoothed sunspot data, we need to predict 6 months ahead from the last existing smoothed sunspot number due to the dependence of each smoothed sunspot datum on the 12 raw monthly sunspot numbers surrounding it. If the smoothed sunspot data is predicted 48 months ahead, the final value will apply to 42 months in the future. All results given here are without this 6 month lag removed. To calculate the normalized prediction error E, we predicted the sunspot numbers for the period 1950-1970 and compared the predictions to the actual sunspot numbers for that period.

To make the most reliable predictions with the first order direct method, we found the number of nearest neighbors to use which gives the lowest E. From the graph in Figure 7, the best number of neighbors is 70, using a time step of 36 months. For the first order iterated method, we found the best number of neighbors to be 25 for a time step of 36 months. However, for the iterated method, there was little variation in the normalized errors found from using 25 nearest neighbors up to using 100 nearest neighbors.

Once these optimal numbers of nearest neighbors were found, we used these numbers in comparing the predictions using each method. The results are shown in Figure 8. The zeroth-order method is much less reliable than either of the first-order methods, becoming as ineffective as the average for a prediction of 3 years. The direct prediction gives E = 1 after about 4 years. The direct prediction is more reliable than the first-order iterative prediction, probably due to the noise in the data. Consequently, we will use the direct first-order local-linear method of forecasting exclusively throughout the rest of the paper.

The quality of the predictions varies depending on where on the cycle the prediction is made. The trajectories become tangled near the origin in phase space (a minimum of the sunspot cycle). Consequently, predictions from a

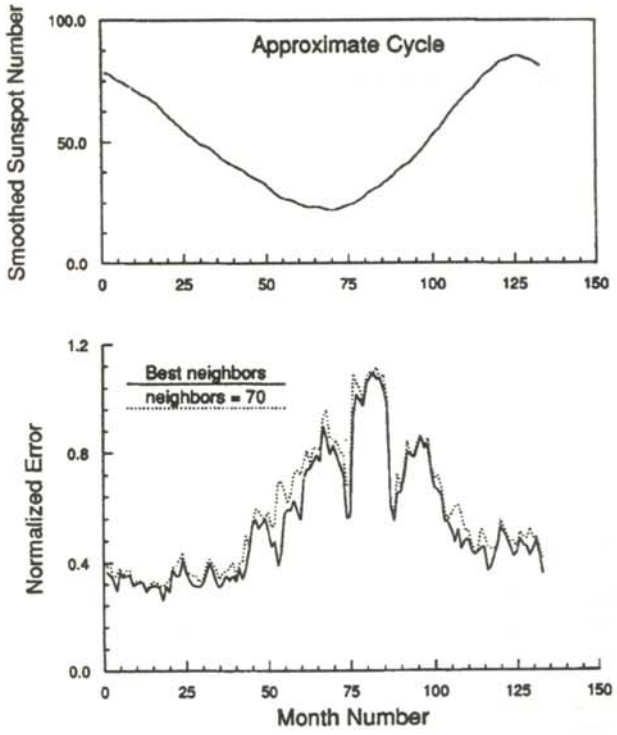

Figure 9
A comparison of the use of 70 neighbors in the first-order direct prediction method with the best number of neighbors to use at various points in the solar cycle. The top graph is a sample cycle, for reference.

minimum are less accurate than those from a maximum. To obtain better predictions, we calculated the optimal number of neighbors to use at each point along the 133 month cycle, for a prediction time of 24 months. The best number of neighbors to use increased near a minimum, but did not yield significantly better results than choosing the number of nearest neighbors to be 70, as shown in Figure 9.

We used the direct local-linear method with 70 nearest neighbors to forecast the current solar cycle, and the beginning of the next solar cycle, forecasting from October 1990 to December 1997. The results of this forecast are shown in Figure 9 and in Table 1. The error bars in this figure are the average positive and negative errors computed from predictions of previous smoothed sunspot numbers from similar positions on the sunspot cycle.

Deterministic chaos provides a foundation from which short-term forecasts of the smoothed monthly sunspot numbers can be made. These forecasts are useful for predictions up to four years head, as long as prediction is not attempted from a minimum in the solar cycle.

ACKNOWLEDGEMENTS

Computational resources for the calculations were provided by the Department of Physics at the University of Alaska Fairbanks, the University of Alaska Academic Computing Department, and the San Diego Supercomputer Center. Other assistance was provided by Dean Prichard, Kirk Hogenson, John V. Olson, and by my sponsor Channon Price.

† This research was funded by NSF through the Physics summer intern program at the Geophysical Institute in Fairbanks, Alaska.

REFERENCES

1. J.C.H. Hsü, trans., The Mendes Collection of Shang Dynasty Oracle Bones, Royal Ontario Museum, Toronto, Canada ,1972.

2. D.J. Schove, ed. in: Sunspot Cycles, Hutchinson Ross, Stroudsburg, 1983.

3. G. Galileo, Discoveries and Opinions of Galileo, S. Drake, ed. and trans., Doubleday, New York, 1957.

4. H.Schwabe, *Solar Observations During 1843* in: Early Solar Physics, A.J. Meadows, ed. and trans., Pergamon Press, London, 1970 p. 95.

5. A. Schuster, *On the Periodicity of Sunspots*, Philos. Trans. R. Soc. London 206,1906 p. 69.

6. M. Waldmeier, The Sunspot-Activity in the Years 1610-1960, Schulthess, Zürich, 1961.

7. O.R. White in: Geophysical Predictions, National Academy of Sciences, Washington D.C., 1978, p. 69.

8. A.G. McNish and J.V. Lincoln, *Prediction of Sunspot Numbers*, EOS Transactions, AGU 30, 1949, p. 673.

9. C.A. Wood, *Solar Activity Prediction for Cycle 21*, in: Solar-Terrestrial Predictions Proceedings, 3, U.S. Dept. of Commerce, Boulder, 1980, p. A58.

10. S.G. Kapoor, S.M. Wu, *Developing Forecasting Charts for Sunspot Numbers*, JGR, 87,1982, p. 9.

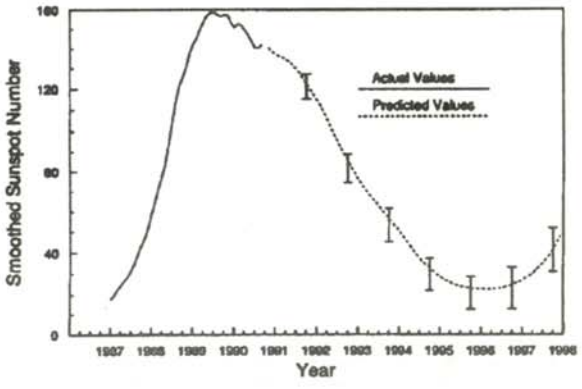

Figure 10
The predicted conclusion to the current sunspot cycle. Errors given are the average positive and negative errors from predicting known cycles from the same position in the solar cycle.

11. W. Gleissberg, *The Probable Behavior of Sunspot Cycle 21*, Solar Phys., 21, 1971, p. 240.

12. D.G. King-Hele, *Prediction of Future Sunspot Cycles*, Nature, 199, 1963, p.226.

13. J. Kurths, and A.A. Ruzmaikin, *On Forecasting the Sunspot Numbers*, Solar Phys., 126, 1990, p. 407.

14. M.D. Mundt, W.B. Maguire, and R.R.P. Chase, *Chaos in the Sunspot Cycle: Analysis and Prediction*, JGR, 96, 1991, p. 1705.

15. *Junk in Space: What Goes Up*, The Economist, April 28, 1979, p.113.

16. E.W. Maunder, *The Prolonged Sunspot Minimum, 1645--1715*, British Astron. Assoc. Jour., 32, 1922, p. 140.

17. J.A. Eddy, *The Maunder Minimum*, Science, 192, 1976, p. 1189.

18. J.B. Ramsey, and H.J. Yuan, *Bias and Error bars in Dimension Calculations and Their Evaluation in Some Simple Models*, Phys. Lett., A134, 1989, p.287.

19. J. Theiler, *Spurious Dimension From Correlation Algorithms Applied to Limited Time-series Data*, Phys. Rev., A34, 1986, p. 2427.

20. J.W. Havstad and C.L. Ehlers, *Attractor Dimension of Nonstationary Dynamical Systems From Small Data Sets*, Phys. Rev., A39, 1989, p. 845.

21. J.D. Farmer and J.J. Sidorowich, *Exploiting Chaos to Predict the Future and Reduce Noise*, Evolution, Cognition, and Learning}, Y.C. Lee, ed., World Scientific, Singapore, 1988. p. 277.

22. E.N. Lorenz, *Deterministic Nonperiodic Flow*, J. Atmos. Sci., 20, 1963, p.130.

23. B.B. Mandelbrot, Fractals --- Form, Chance, and Dimension, Freeman, San Francisco, 1977.

24. A. Wolf, J.B. Swift, H.L. Swinney, and J.A. Vastano, *Determining Lyapunov Exponents From a Time Series*, Physica, 16D, 1985, p. 285.

25. J.P. Eckmann, D. Ruelle, S. Ciliberto, and S. Oliffson Kamphorst, *Lyapunov Exponents From Time Series*, Phys. Rev., A34, 1986, p. 4971.

26. R.L. Devaney, Chaos, Fractals, and Dynamics: Computer Experiments in Mathematics,Addison-Wesley, Menlo Park, 1990.

27. J. Gleick, Chaos: Making a New Science, Viking, New York, 1987.

28. R. Bergé, Y. Pomeau, and C. Vidal, Order Within Chaos: Towards a Deterministic Approach to Turbulence,Hermann, Paris, 1984.

TABLE 1
Predicted Smoothed Sunspot Numbers through 1997

Month/Year	Number	Month/Year	Number	Month/Year	Number
10/90	140.2	3/93	68.8	8/95	23.4
11/90	138.4	4/93	66.7	9/96	23.0
12/90	137.0	5/93	64.8	10/95	22.6
1/91	136.2	6/93	62.6	11/95	22.6
2/91	135.5	7/93	60.6	12/95	22.7
3/91	134.4	8/93	58.5	1/96	22.5
4/91	133.2	9/93	56.3	2/96	22.6
5/91	131.7	10/93	54.3	3/96	22.7
6/91	129.6	11/93	52.4	4/96	22.7
7/91	127.5	12/93	50.4	5/96	22.9
8/91	125.0	1/94	48.4	6/96	23.2
9/91	122.5	2/94	46.2	7/96	23.7
10/91	119.7	3/94	44.0	8/96	24.2
11/91	117.1	4/94	41.8	9/96	24.8
12/91	114.8	5/94	39.6	10/96	25.6
1/92	112.0	6/94	37.5	11/96	26.1
2/92	108.9	7/94	35.7	12/96	26.9
3/92	105.5	8/94	34.2	1/97	28.1
4/92	101.7	9/94	32.8	2/97	29.0
5/92	98.2	10/94	31.3	3/97	30.1
6/92	94.9	11/94	29.8	4/97	31.7
7/92	91.5	12/94	28.6	5/97	33.5
8/92	88.5	1/95	27.4	6/97	35.2
9/92	85.4	2/95	26.6	7/97	37.0
10/92	82.4	3/95	25.9	8/97	38.8
11/92	79.3	4/95	25.1	9/97	41.4
12/92	76.2	5/95	24.5	10/97	44.4
1/93	73.6	6/95	24.0	11/97	47.8
2/93	71.1	7/95	23.7	12/97	51.5

29. N. Gershenfeld, *An Experimentalist's Introduction to the Observation of Dynamical Systems*, Directions in Chaos vol. 2, H. Bai-lin, ed., World Scientific, Singapore, 1988, p. 310.

30. N.H. Packard, J.P. Crutchfield, J.D. Farmer, and R.S. Shaw, *Geometry From a Time Series*, Phys. Rev. Lett., 45, 1980, p. 712.

31. F. Takens, *Detecting Strange Attractors in Turbulence*, Dynamical Systems and Turbulence, Vol. 898 Lecture Notes in Mathematics, D.A. Rand, and L.S. Young, eds., Springer, New York, 1981, p. 366.

32. P. Grassberger and I. Procaccia, *Characterization of Strange Attractors*, Phys. Rev. Lett. 50, 1983, p. 346.

33. A.M. Fraser and H.L. Swinney, *Independent Coordinates for Strange Attractors from Mutual Information*, Phys. Rev., A33, 1986, p. 1134.

34. W. Liebert and H.G. Schuster, *Proper Choice of the Time Delay for the Analysis of Chaotic Time Series*, Phys. Lett., A142, 1989, p. 107.

35. J.D. Farmer and J.J. Sidorowich, *Predicting Chaotic Time Series*, Phys. Rev. Lett., 59, 1987, p. 845.

FACULTY SPONSOR

Dr. Channon P. Price
Physics Department
University of Alaska Fairbanks
Fairbanks, AK 99775-1320

The Journal of Undergraduate Research in Physics

The **Journal of Undergraduate Research in Physics** is the journal of Sigma Pi Sigma and the Society of Physics Students. It is published by the Physics Department of Guilford College, Greensboro NC. Inquiries about the journal should be sent to the editorial office.

Editorial Office -

Physics Department
Guilford College
Greensboro, NC 27410
919-316-2279 (voice)
919-316-2951 (FAX)

Editor -

Dr. Rexford E. Adelberger
Professor of Physics
Department of Physics
Guilford College
Greensboro, NC 27410
ADELBERGERRE@RASCAL.GUILFORD.EDU

The Society of Physics Students

National Office -

Dr. Donald Kirwin, Executive Director
Dr. Edwin Goldin, Associate Director
Society of Physics Students
American Institute of Physics
1825 Connecticut Avenue, N.W.
Suite 213
Washington, DC 20009
202-232-6688

President of the Soceity -

Dr. Jean Krisch
Department of Physics
University of Michigan

President of Sigma Pi Sigma -

Dr. Reuben James
Department of Physics
SUNY College at Oneonta